Influence of atmospheric water vapor on infrared measurement systems in central receiver systems

École Nationale d'Arts et Métiers

Institute of Solar Research, German Aerospace Center

Romain Larue

Supervisors: Simon Caron,
Institute of Solar Research, German Aerospace Center

Adel Olabi,
École Nationale d'Arts et Métiers

Examiners: Adel Olabi,
École Nationale d'Arts et Métiers

Aurélien Grolet,
École Nationale d'Arts et Métiers

Abstract

This thesis investigates a new system that can measure the temperature and emittance of the receiver in a solar tower power plant. These measurements are important for the efficiency and maintenance of the receiver. The system uses a multispectral camera that works in the short wavelength infrared spectrum. It uses two filters that are sensitive to water vapor in the air, which helps to reduce the effect of solar reflections on the signal. The system is based on ratio thermography, which is a method that compares the signals from different wavelengths.

The aim of this report is to assess the influence of atmospheric water vapor absorption on the precision and accuracy of infrared temperature measurements in the context of solar towers. It shows that the atmosphere plays a significant role in the measurement accuracy, the most important being absolute humidity, and uses methods to correct errors due to the atmosphere.
It concludes that SWIR ratio thermography is only suitable with specific conditions, for example at dusk at the tower of Cerro Dominador.

Acknowledgements

I am very grateful to the Institute for giving me the chance to do my master thesis with them. I am deeply grateful to my supervisor Simon Caron for his dedication and guidance during this thesis, which has been of great value to me. I also thank my academic supervisor Adel Olabi and examiner Aurélien Grolet for their roles and responsibilities. I thank the DLR team for their support and friendliness. I also acknowledge the Hauts de France region for awarding me a MERMOZ scholarship.

Nomenclature

Abbreviations

AM	Air Mass
CSP	Concentrated Solar Power
DOE	Design Of Experiments
IR	Infrared
LWIR	Long Wavelength Infrared (7-14 µm)
MLS	Mid Latitude Summer
MODTRAN	MODerate resolution atmospheric TRANsmission
NB	Narrow Band filter
NGCF	Non Greybody Compensation Factor
SWIR	Short Wavelength Infrared (0.9 – 2.5 µm)

Physics constants

b	Wien's displacement constant	$2898\ \mu m.K$
h	Planck constant	$6.62607015 \times 10^{-34}$ J · Hz^{-1}
c	Speed of light in vacuum	$299\ 792\ 458\ m \cdot s^{-1}$
$c_1 = 2\pi hc^2$	First radiation constant	
$c_2 = \frac{hc}{k_B}$	Second radiation constant	0.014387752 m · K
k_B	Boltzmann constant	$1.380649 \times 10^{-23}\ J \cdot K^{-1}$
σ	Stefan–Boltzmann constant	$5.670374419 \times 10^{-8}$ W · m^{-2} · K^{-4}

Symbols

Note: T_{air}, P_{atm}, RH are all specified at ground altitude (local weather station)

Parameter	Unit	Description
AH	$\frac{g}{m^3}$	Absolute Humidity
atm		Atmospheric parameters (atmospheric pressure, air temperature, humidity) varying with altitude and estimated via ground sensors
Cx	Sun	Concentration factor
H_0	km	Ground altitude
$H_{1\ alt}$	km	Heliostat altitude
$H_{2\ alt}$	km	Receiver altitude
L_2	km	Length Path 2
L_3	km	Length Path 3
M	$\frac{W}{m^2}$	Radiant Exitance or irradiance
$M_{BB\ abs}$	$\frac{W}{m^2}$	Blackbody Radiant Exitance of the absorber
$M_{BB\ chip}$	$\frac{W}{m^2}$	Blackbody Radiant Exitance of the sensor chip

M_{BB}	$\frac{W}{m^2}$	Radiant Exitance of a blackbody
M_{sun}	$\frac{W}{m^2}$	Extraterrestrial Solar irradiance
M_λ	$W\ m^{-2}\ nm^{-1}$	Spectral Radiant Exitance
$NGCF$	$-$	Non Greybody Compensation Factor
OD_i	$-$	Optical Depth path 1, filter i
P_{atm}	hPa	Atmospheric Pressure
QE	$-$	Quantum Efficiency of the sensor
RH	%	Relative Humidity
S	$arbitrary$	Radiometric Signal
S_{calib}	$arbitrary$	Calibration Radiometric Signal
SR	$-$	Signal Ratio
SR_{meas}	$-$	Measured Signal Ratio, without NGCF correction
SZA	$^\circ$	Solar Zenith Angle
T_{abs}	$°C$	Absorber Temperature
T_{air}	$°C$	Ambient Temperature
T_{chip}	$°C$	Temperature of the sensor chip
T_{guess}	$°C$	Temperature estimation
ΔT	$°C$ (K for calculus)	Temperature error
$\frac{\Delta T}{T}$	%	Temperature relative error

Greek symbols

α_λ	%	Spectral absorptance
ϵ	$-$	Emittance of the absorber's surface
$\Delta\epsilon_i$	pp	Emittance error, filter i
$\frac{\Delta\epsilon_i}{\epsilon_i}$	%	Emittance relative error, filter i
ϵ_i	%	Absorber emittance estimation, filter i
$\epsilon_{i\,\lambda}$	%	Spectral emittance of the absorber's surface, filter i
τ_1	%	Atmospheric transmittance of path 1
τ_2	$-$	Atmospheric transmittance of path 2
τ_3	$-$	Atmospheric transmittance of path 3
$\tau_{i\,\lambda}$	%	Spectral atmospheric transmittance of path i
ρ_{mirror}	$-$	Reflectance of the mirrors
θ	$^\circ$	Incidence angle between the incident solar ray and the normal of the mirror

Indices

atm	atmosphere
abs	absorber
BB	blackbody
λ	spectral

Table of Contents

List of figures

List of tables

Introduction

Solar power is instrumental in the fight against climate change. The most widely adopted solar technology is photovoltaic power. However, Concentrated Solar Power (CSP) has characteristics that make it an interesting alternative solution [1].

CSP uses a field of solar tracking mirrors to focus sunlight, i.e., Direct Normal Irradiance (DNI) on a smaller thermal receiver. Concentrated solar radiation brings heat to the receiver, which offers a broad range of uses, including 24/7 baseload electricity generation with long duration thermal storage, industrial process heat, or synthetic fuel production [2].

Among CSP technologies, line-focusing and point-focusing configurations can be found. Line-focusing technologies focus sunlight onto a line. Parabolic troughs and Linear Fresnel reflectors are the main line-focusing technologies. Point-focusing technologies focus sunlight onto a point. Parabolic dishes and tower configurations are the main point-focusing technologies [3].

In a tower configuration, a ground-based heliostat field, surrounding the tower, concentrates solar radiation onto a thermal receiver mounted at the top of the tower. Heliostats are equipped with two axis trackers, allowing them to follow the Sun trajectory along azimuth and elevation angles.

Statement of the problem

Knowing the receiver surface temperature of a solar power tower is key to ensure maximum operating efficiency - which is positively correlated to the receiver's temperature - without degrading the receiver by overheating it. Knowing the receiver emittance allows monitoring the health of the coated receiver surface and helps deciding whether recoating may be required to maintain the receiver opto-thermal efficiency.

Current solar power tower technology relies on commercial Long Wavelength InfraRed (LWIR, 7-14 μm) cameras [4] to determine the temperature of the receiver's surface thanks to the infrared radiation it emits according to Planck's law of blackbody radiation. Despite their high price, mainly influenced by the telephoto lens required for remote sensing at a fairly long range (approx. 350 meters), they are the main way to measure the receiver surface temperature in real time.

A Short Wavelength InfraRed (SWIR, 0.9 – 2.5 μm) prototype camera system is being developed to cross-check the accuracy of LWIR cameras and measure the emittance of the receiver's surface, one of the important health parameters. However, it may be hampered by shortwave solar radiation, which interferes with the infrared measurement signal [5].
LWIR cameras are less subject to this problem, because the amount of solar radiation which is reflected by the black coated thermal receiver at these wavelengths (8-14 μm) is less significant.

To solve this issue, the SWIR prototype camera is equipped with a wheel of narrow-band filters that match some atmospheric absorption bands (1.4 & 1.9 μm). However, these absorption bands are primarily caused by atmospheric water vapor, making the measurements sensitive to weather conditions. The transmittance of the atmosphere can be obtained by a series of MODTRAN simulations for various atmospheric conditions, using accessible weather parameters at ground level, such as air temperature T_{air}, relative humidity RH, atmospheric pressure P_{atm}. Ratio thermography with a Non Graybody Correction Factor (NGCF) is applied on oxidized or black coated receiver surfaces to retrieve temperature and emittance maps, minimizing atmospheric influences.

Another way of solving the solar reflection problem is to operate these cameras at dusk, while the receiver is still warm, typically above 300 °C. In these conditions, solar blindness is fulfilled, as all

heliostats are defocused. Therefore, another pair of filters is studied (1.64; 2.09 μm) corresponding to H and K atmospheric windows in the Johnson Morgan UBV photometric system [6]). These filters correspond to wavelengths at which the atmosphere is mainly transparent, maximizing black body thermal radiation received by the camera and significantly reducing atmospheric influences.

The aim of this report is to assess the influence of atmospheric water vapor absorption on the precision and accuracy of infrared temperature measurements (SWIR, LWIR) in the context of solar towers.

Statement of hypothesis of research questions

A Gray body hypothesis is made for the black coated or oxidized receiver surface [7] and a Non Graybody Compensation Factor is introduced for atmospheric water bands [8].

Infrared cameras are considered to be located on the ground, within the heliostat field.

The atmospheric composition reference is based on a Mid-Latitude Summer (MLS) setting.

Further atmospheric parameters are first deemed secondary (SWIR: aerosols; LWIR: CO_2, O_3).

Review of related literature

LWIR State of the art

Eitan et al. [9] use thermographic LWIR cameras to monitor the temperature of the central receiver. They use an inverse thermal model to deduce the concentrated solar flux reaching the receiver's surface. The LWIR cameras were protected in a sealed enclosure with a germanium window, as glass blocks LWIR radiation, and "located in the solar field a few hundred meters away from the receiver." They develop a method to calibrate the LWIR cameras by setting the receiver to a known and constant temperature, without concentrated solar radiation, and measuring the radiation received by the cameras. They obtain reading errors up to 8 °C from uncertainties in the transmittance of the atmosphere as a function of humidity and up to 4 °C from the camera's chip temperature.

Ratio thermography

Savino et al. [10] investigate the method to choose pairs of narrow-band filters for temperatures up to 500 °C with experiments and spectral simulations. In the Long Wavelength domain (7-14 μm), they find that ratio thermography is not sensitive enough for accurate measurements. In the Mid Wavelength domain (3-5 μm), they obtained a temperature error of less than 5 % with a pair of filters, due to the gray body hypothesis, which states that the emittance of a surface is constant regardless of the wavelength.

Araújo [11] reviews different ratio thermography techniques and concludes that dual-wavelength thermography is limited to the gray hypothesis, which means that with only two filters, emittances of the receiver at the corresponding two wavelengths must be constant, or at least their ratio must be known. Araujo notes that with more than two wavelengths, mathematical complexity increases dramatically without much improvement in the accuracy of the readings.

Hijazi et al. [8] develop a dual-wavelength technique that does not rely on the graybody hypothesis. They introduce the non-graybody compensation factor (NGCF). Using a non-graybody, they show this technique can achieve a better accuracy than a gray body hypothesis if the surface is not gray.

Solar blind thermography

Pfänder et al. [12] investigate the solar blind technique by optimizing the filter wavelength for temperature reading for a target temperature between 400 °C and 1200 °C. A compromise was made between sunlight reflection attenuation and black body infrared signal transmission. This was possible thanks to the low transmittance of glass mirrors at the studied wavelength (4.56 μm). They found that the low transmittance of glass mirrors allows more accurate temperature readings.

State of the art

Electromagnetic radiation

Different types of radiation, such as visible light, ultraviolet, and infrared, can be seen as waves of electric and magnetic fields. These waves are called electromagnetic waves. They have some properties that depend on how they move in space and time. For example, the distance between two consecutive peaks of a wave is called the wavelength, λ. The number of times a wave repeats itself in one second is called the frequency, ν. The product of the wavelength and the frequency is the speed of the wave, c. This speed is different for different types of waves. For instance, sound waves need matter to exist and travel slower than light waves, which can travel in a vacuum. They also differ by the amount of energy a photon carries, expressed by Planck relation in Eq. (1) [13]. The shape of a wave can be described by a mathematical function, such as a sine function.

$$E = \frac{hc}{\lambda} \tag{1}$$

The IR spectrum is a small part of the electromagnetic spectrum that is used for IR imaging (Figure 1). There are three main ranges for thermography: the long-wave (LW) range from about 8 to 14 µm, the mid-wave (MW) ranges from about 3 to 5 µm, and the short-wave (SW) range from 0.9 to 1.7 µm. These ranges have different cameras for them.

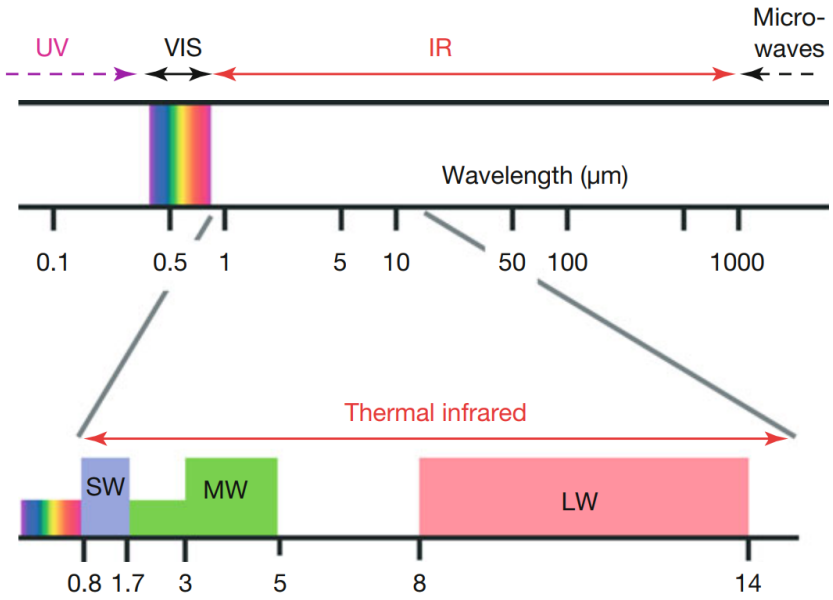

Figure 1: Electromagnetic spectrum [14, p. 10]

Blackbody radiation

There are many sources of electromagnetic radiation in nature. The most important one for thermography is thermal radiation. Thermal radiation means that any body or object with a temperature T > 0K (-273.15 °C) emits electromagnetic radiation. The amount and type of radiation depend on temperature and material properties. For temperatures that we usually see in nature and technology, this radiation is in the thermal IR range.

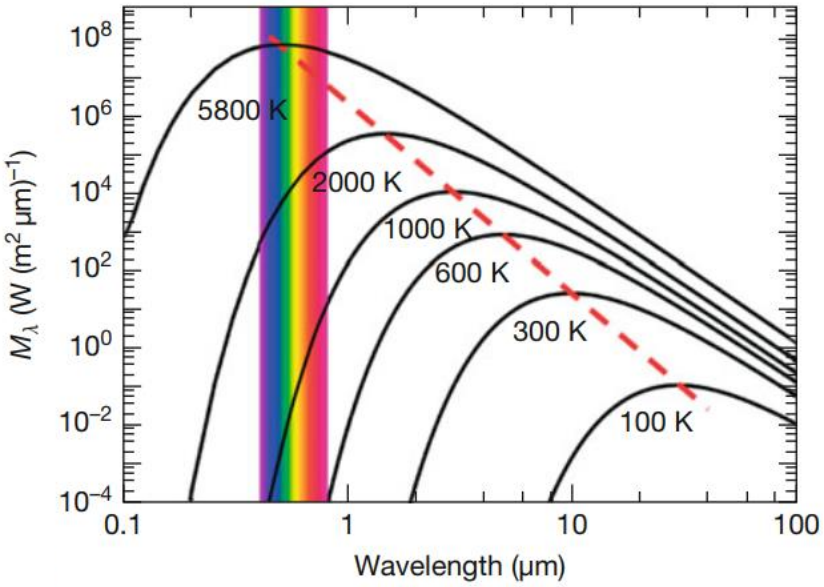

Figure 2: Blackbody radiation [14, p. 25]

The amount of radiation that a blackbody emits at different wavelengths follows Planck's radiation law (Eq. 2). The higher the temperature of the object, the more radiation it emits (Figure 2) [15].

Planck's law, expressed in radiant exitance:

$$M_{\lambda\,BB}(\lambda, T) = \frac{c_1}{\lambda^5} \frac{1}{\exp\left(\frac{c_2}{\lambda T}\right) - 1} \tag{2}$$

The exitance, which is a measure of spectral radiation, varies with the wavelength as shown in Figure 2, with a maximum depending on the temperature, following Wien's displacement law [16], (Eq. 3):

$$\lambda_{peak} = \frac{b}{T} \tag{3}$$

In IR imaging, only a part of the blackbody radiation spectrum is often used. Two ways to measure the amount of radiation in a certain range of wavelengths exist. The Stefan–Boltzmann law gives the total radiation for the whole spectrum, from zero to infinity, while band emission depends on the limits of the range.

The amount of radiation an object emits can be calculated by an integration of Planck's law over the wavelength (Eq. 4):

$$M(T) = \int_0^\infty M_{\lambda\,BB}(\lambda, T).\, d\lambda \tag{4}$$

Stefan-Boltzmann's Law (Eq. 5) is the integral of Planck's law from 0 to infinite wavelength.

$$M(T) = \sigma\, T^4 \tag{5}$$

This law is not practical, because no sensor has such a range of detection. Unlike the Stefan-Boltzmann law, the Sakuma-Hattori law, the integral is bounded to a specific wavelength interval. A camera only

sees the sum of spectral radiations for all wavelengths inside a spectral window. The Sakuma-Hattori equation [17] , (Eq. 6) provides an approximation of the signal produced by a camera sensor as function of its temperature:

$$S(T) = \frac{C}{\exp\left(\frac{c_2}{AT}\right) - 1} \tag{6}$$

Material properties

The properties of the material affect how electromagnetic radiation behaves when it meets it. The radiation can be transmitted, reflected, or absorbed. The fraction of radiation that goes through the medium is τ, where τ is the transmittance of the medium. The fraction of radiation that bounces off the surface of the medium is ρ, where ρ is the reflectance of the medium. The fraction of radiation that is absorbed by the medium is related to the absorption coefficient α of the medium. According to the conservation of energy, the amount of incident radiation equals the sum of transmitted, reflected, and absorbed radiation, i.e., the sum of their fractions is equal to one (Eq. (7)).

$$\rho + \alpha + \tau = 1 \tag{7}$$

According to Kirchhoff's law, any object absorbs and emits the same amount of radiation at a given wavelength. This can be expressed as:

$$\epsilon_\lambda(\lambda) = \alpha_\lambda(\lambda) \tag{8}$$

Emittance

Emittance is a measure of how much thermal radiation an object can emit. A perfect emitter, called a blackbody, has an emittance of 1 because it absorbs and emits all the radiation it receives. However, no real object is a perfect emitter. Emittance is therefore needed to calculate how much radiation it actually emits (Eq. (9)).
Spectral emittance is defined as the ratio of radiant exitance leaving a surface to the radiance exitance of a blackbody at the same temperature [14, p. 31]:

$$\epsilon_\lambda(\lambda, T) = \frac{M_\lambda(\lambda, T)}{M_{\lambda\,BB}(\lambda, T)} \tag{9}$$

The gray body hypothesis states that emittance of a surface does not vary regardless of the selected wavelength (Figure 3).

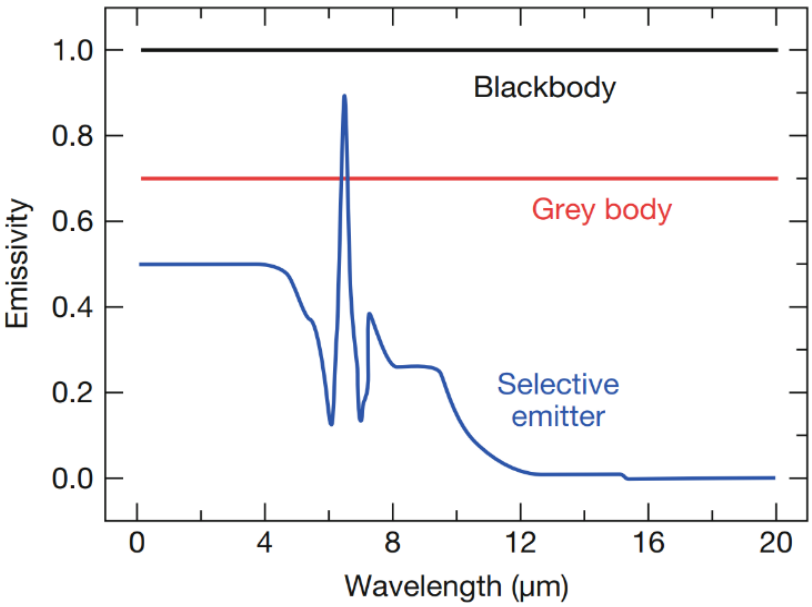

Figure 3: Emittance spectrums of a blackbody, a grey body, and a selective emitter [14, p. 33]

Band emittance is a measure of the amount of spectral radiation inside a wavelength band an object emits compared to a blackbody in the same wavelength band [18]:

$$\epsilon = \frac{\int_{\lambda_1}^{\lambda_2} \epsilon_\lambda(\lambda, T)\, M_{\lambda\, BB}(\lambda, T)\, d\lambda}{\int_{\lambda_1}^{\lambda_2} M_{\lambda\, BB}(\lambda, T)\, d\lambda} \quad (10)$$

Atmospheric transmittance

The atmosphere is a layer of gases that surrounds the Earth and protects it from the radiation of the sun. The composition of the atmosphere varies depending on the altitude, but it mainly consists of nitrogen (78% of dry mole fraction), oxygen (21%), argon (0.9%), carbon dioxide (0.04%) and water vapor. The atmosphere affects the amount of solar radiation that reaches the Earth's surface, as some of it is reflected, scattered, or absorbed by atmospheric particles and molecules. This is quantified by the atmospheric transmittance of solar radiation, which depends on factors such as the wavelength of the radiation, the angle of incidence, the cloud cover and the aerosol concentration.

Figure 4 shows bands of low transmittance in the SWIR range except for absorption bands at 1.4 and 1.9 microns, which indicate that the absorbing molecules are blocking some wavelengths of light more than others. These bands correspond to the vibrational and rotational modes of the molecules, which are excited by the infrared radiation.

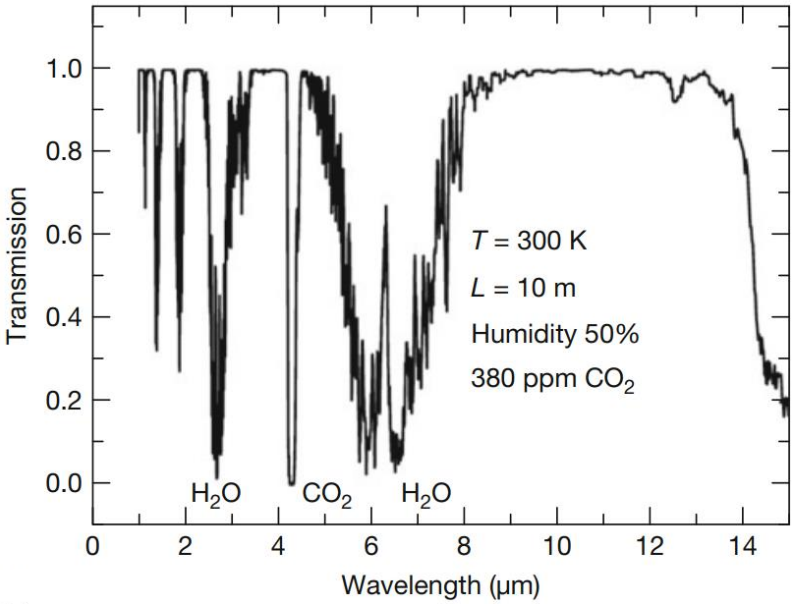

Figure 4: Spectral transmittance of atmosphere [14, p. 53]

Atmosphere has a high transmittance in most of the LWIR range. However, as shown in Figure 5, solar radiation lowers as wavelength increases above 500 nm. This means that sun radiation in the LWIR range is low while radiation from the absorber is easily transmitted through air.

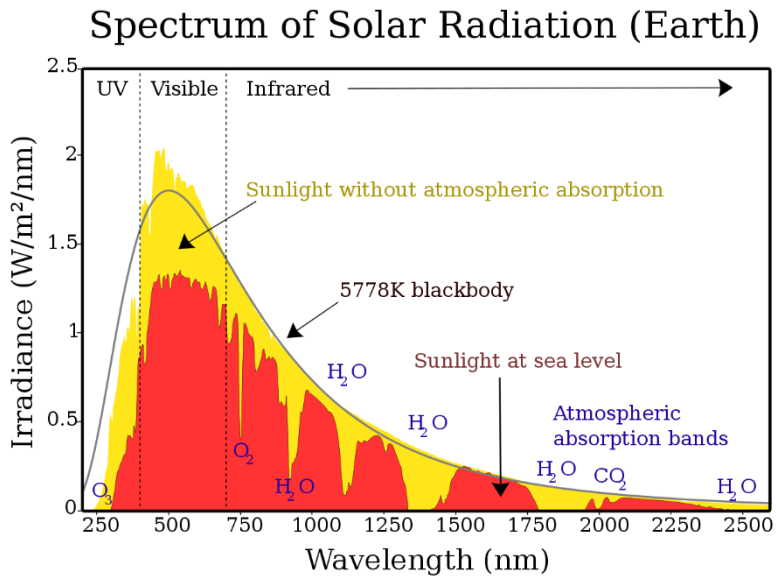

Figure 5: spectrum of solar radiation [19]

Figure 6 shows that water vapor concentration decreases rapidly with altitude, reaching near-zero values above 10 kilometers. This means that atmospheric transmittance increases with altitude, as there are fewer molecules and particles to absorb or scatter radiation.

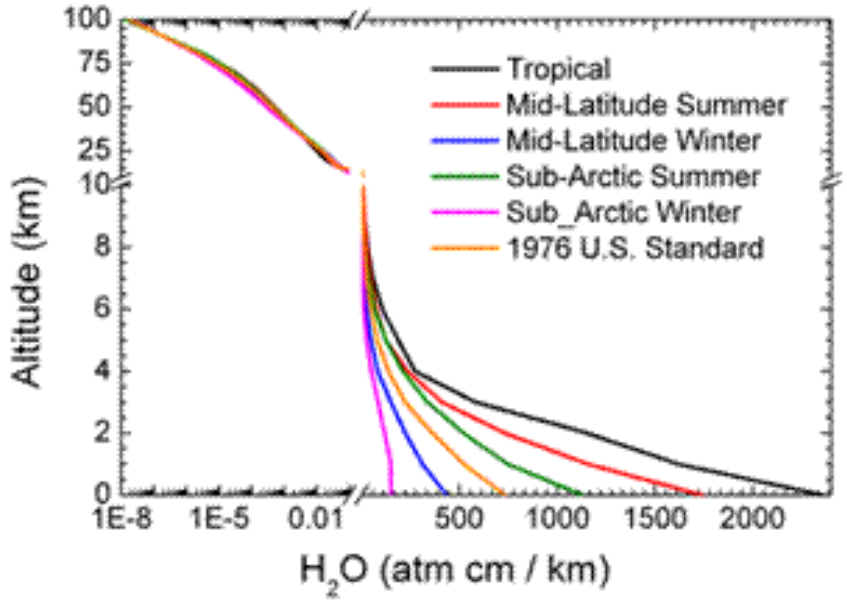

Figure 6: altitude profile of water vapor [20]

Solar blindness

Solar blindness defines conditions under which concentrated solar radiation is not interfering with temperature measurements [12]. Different solar blindness strategies can be adopted or combined: heliostat defocus (aiming mirrors away from the absorber), mirror absorption, atmospheric absorption, or receiver absorption. Solar blindness is wavelength dependent and requires the selection of adequate bandpass filters.

Infrared thermography

A contactless method for surface temperature measurement is infrared thermography. It uses a thermal camera to capture the thermal radiation that an object emits in the infrared range. It can create a full map of the object's temperature without damaging it, unlike contact methods that only measure one point at a time. Many industries have adopted this method in recent years [10]. However, IR thermography often depends on knowing the emittance of the object. The emittance of a surface may vary with temperature, wavelength, view angle and its degradation, so it is hard to estimate it even with some prior information.

Methodology

Radiometric chain

The radiometric chain is a series of interactions that take place on the path of the radiation to finally reach the camera sensor and produce a signal. The typical radiometric chain for a solar tower in shown in Figure 7. Radiation from the Sun to the heliostat field (path 1) is partially absorbed by the atmosphere. This absorption varies with the amount of water vapor in the atmosphere and the Sun position (Solar Zenith Angle). The remaining radiation is partially reflected by heliostats to the absorber (path 2) and undergoes a new partial absorption by the atmosphere. On path 3, a fraction of radiation received by the absorber is reflected to the infrared camera (Solar reflection flux) and undergoes a new partial absorption by the atmosphere. The absorber also emits its own radiation thanks to the black body radiation phenomenon, altered by its emittance (Absorber emission flux). The atmosphere also reflects sun radiation, scatters it, and emits its own radiation due to its temperature.

Atmospheric transmittances are a function of altitude and atmospheric pressure, since the denser the atmosphere, the more radiation is absorbed or scattered. It also depends on path lengths.

Heliostats, the absorber, and the infrared camera are positioned at different altitudes, which will be considered in the simulations.

Instead of considering each heliostat of the field, which may count several thousand units, a single equivalent heliostat will be used in the simulations to simplify the problem.

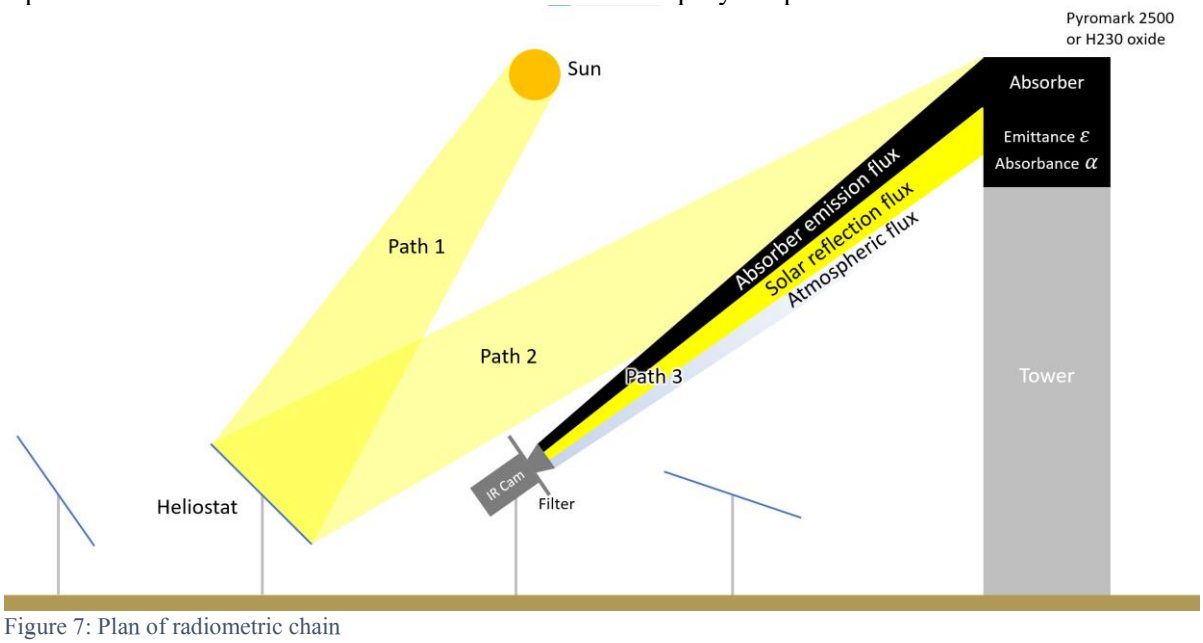

Figure 7: Plan of radiometric chain

In order to measure the temperature of the absorber, the absorber emission flux will be used. All other fluxes are therefore considered as noise that needs to be minimized.

Camera prototype

The camera prototype is composed of a telephoto lens, a filter wheel to choose among 4 filters, and the camera itself (Figure 8).

Radiation enters the telephoto lens, which is used to zoom on the absorber while keeping the camera on the ground for operational and cost purposes. It passes through the selected filter and finally reaches the IR sensor.

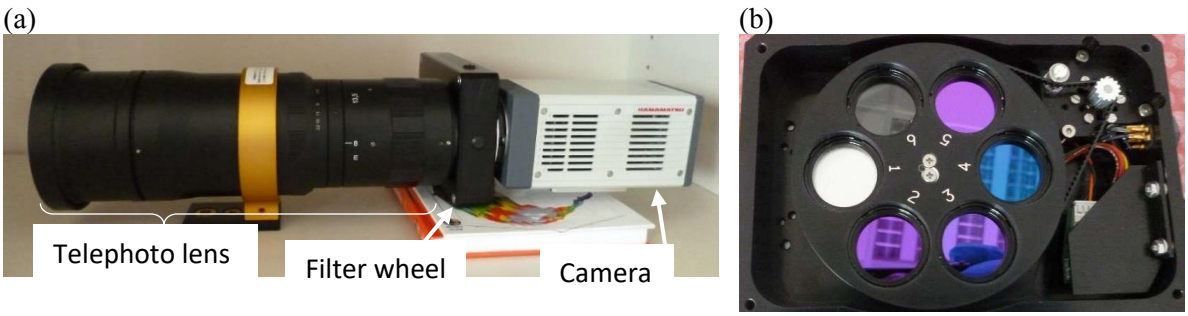

Figure 8: (a): SWIR camera prototype, (b): Filter wheel with 4 filters, a shutter, and a broadband filter

Blackbody radiation of the inside of the camera can be reflected by the filter and reach the sensor. The SWIR camera detector is cooled to -20°C with a thermoelectric unit to make this radiation negligible compared to the absorber radiation.

Radiometric equation

The radiometric equation is used to determine the signal the camera will produce under a set of parameters. For a given pixel, the lumped signal is expressed by Eq. (11).

$$S = \int_{\lambda_{start}}^{\lambda_{stop}} S_{\lambda\, abs}(\lambda).d\lambda + \int_{\lambda_{start}}^{\lambda_{stop}} S_{\lambda\, sun}(\lambda).d\lambda + \int_{\lambda_{start}}^{\lambda_{stop}} S_{\lambda\, atm}(\lambda).d\lambda + \int_{\lambda_{start}}^{\lambda_{stop}} S_{\lambda\, cam}(\lambda).d\lambda \quad (11)$$

With:

- The contribution of the absorber, thanks to its blackbody radiation:

$$S_{\lambda\, abs}(\lambda) = \epsilon_{\lambda}(\lambda, T_{abs}).\tau_{3\,\lambda}(\lambda,\ L_3, atm).M_{\lambda\ BB\ abs}(\lambda, T_{abs}).f_{cam}(\lambda) \quad (12)$$

- The contribution of the solar radiation reflected by the absorber. The incidence angle θ formed by the solar ray and the normal of the mirror is considered close to zero:

$$S_{sun}(\lambda) = C_x[1-\epsilon_{\lambda}(\lambda, T_{abs})].\tau_{1\,\lambda}(\lambda,\ L_1, atm, SZA).\tau_{2\,\lambda}(\lambda,\ L_2, atm).\tau_{3\,\lambda}(\lambda,\ L_3, atm).\rho_{mirror}(\lambda).\cos(\theta).M_{\lambda\ BB\ sun}(\lambda).f_{cam}(\lambda) \quad (13)$$

- The contribution of atmospheric emission. Reflectance is neglected:

$$S_{atm}(\lambda) = [1-\tau_{3\,\lambda}(\lambda,\ L_3, atm)].M_{\lambda\ BB\ atm}(\lambda, T_{air}).f_{cam}(\lambda) \quad (14)$$

- The contribution of camera internal reflection [21]:

$$S_{cam}(\lambda) = [1 - \tau_{\lambda\,\text{filter}}(\lambda)].\,\mathrm{M}_{\lambda\,\text{BB chip}}(\lambda, \mathrm{T}_{\text{chip}}).\mathrm{QE}(\lambda) \quad (15)$$

With the camera response function:

$$f_{cam}(\lambda) = \mathrm{QE}(\lambda)\,\tau_{\text{filter}\,\lambda}(\lambda)\,\tau_{\text{lens}\,\lambda}(\lambda) \quad (16)$$

Spectral database

Spectral data were measured and are provided as input to the simulation software (Figure 9). They will be used as expressed in Eq. (11).

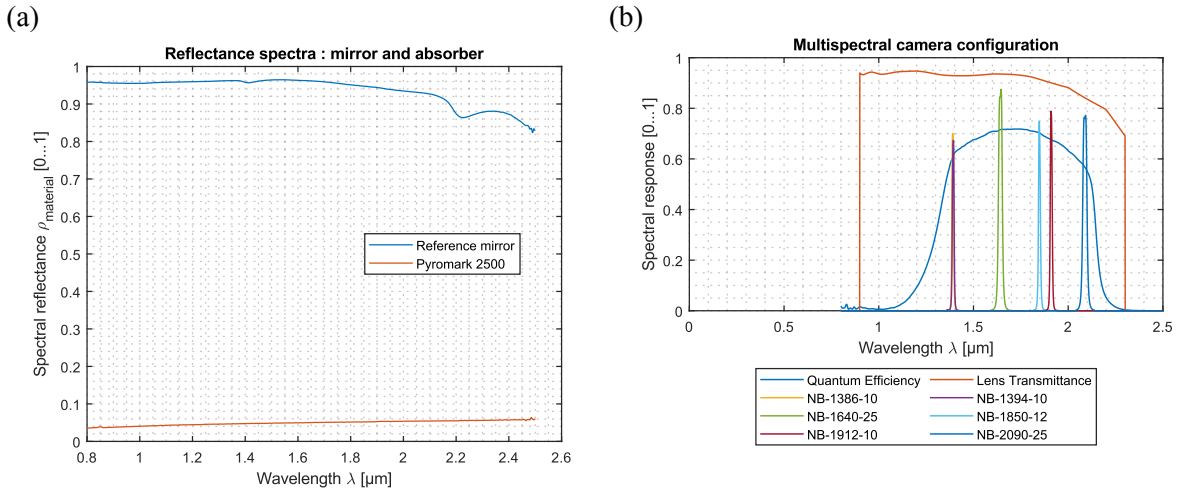

Figure 9: (a): mirror and absorber reflectance, (b): filter transmittances and quantum efficiency

Calibrations

The software uses Planck's law expressed by Eq. (2) to obtain the theoretical signal generated by the camera as function of a blackbody's temperature. This is called a calibration curve (Figure 10 (a)). Ratio calibration curves (Figure 10 (b)) are obtained by taking the ratio of two filter's signals as function of a blackbody's temperature (Eq. (17)):

$$SR(T) = \frac{S_{j\,\lambda}(T)}{S_{i\,\lambda}(T)} \quad (17)$$

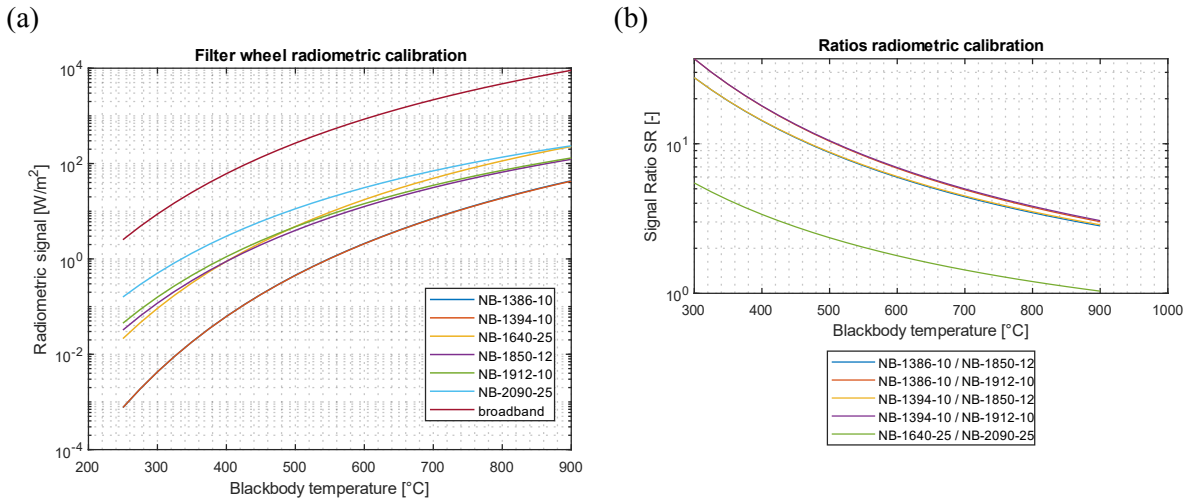

Figure 10: (a): filters calibration curves, (b): ratios calibration curves

Calibration curves are a correspondence between the signal produced by the camera sensor and the temperature of the absorber's surface for ideal conditions, i.e., for a perfect blackbody with $\epsilon = 1$ and no atmospheric absorptance ($\tau = 1$).

MODTRAN simulations

Spectral solar irradiance $M_{\lambda\, BB\, sun}$ and atmospheric transmittances $\tau_{1\lambda}$, $\tau_{2\,\lambda}$, $\tau_{3\,\lambda}$ are obtained with MODTRAN software. It can produce irradiance (Figure 11 (a)) and transmittance (Figure 11 (b)) spectra from various parameters such as path length, atmospheric pressure P_{atm}, air temperature T_{air}, absolute humidity AH at ground level, solar zenith angle.

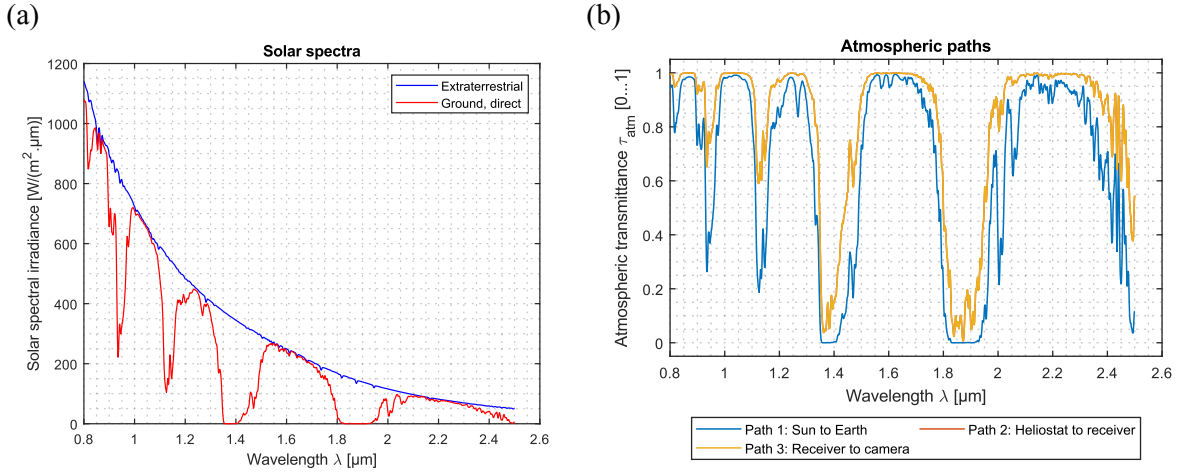

Figure 11: (a): solar spectrum, (b): atmospheric paths transmittances; for the following parameters: $RH = 30\ \%, SZA = 20°, L_2 = 500m, L_3 = 350\ m, P_{atm} = 960\ hPa, T_{air} = 30°C, H_0 = 500\ m$

A design of experiment (DOE) was conducted to build a lookup table for atmospheric transmittance spectra as function of parameters mentioned above, using MODTRAN simulation software.

Forward simulation

A second DOE is conducted for the whole system simulation, taking the same parameters as the previous DOE, and adding parameters relative to the tower operation, i.e., the concentration factor and the absorber temperature. This two-staged DOE allows transmittance simulations to be computed once and used several times, saving computation time.

The forward simulation uses the lookup table to retrieve spectral transmittances $\tau_{1\,\lambda}, \tau_{2\,\lambda}, \tau_{3\,\lambda}$.Terms of Eq. (11) are computed and can be visualized in Figure 12 for a set of parameters.

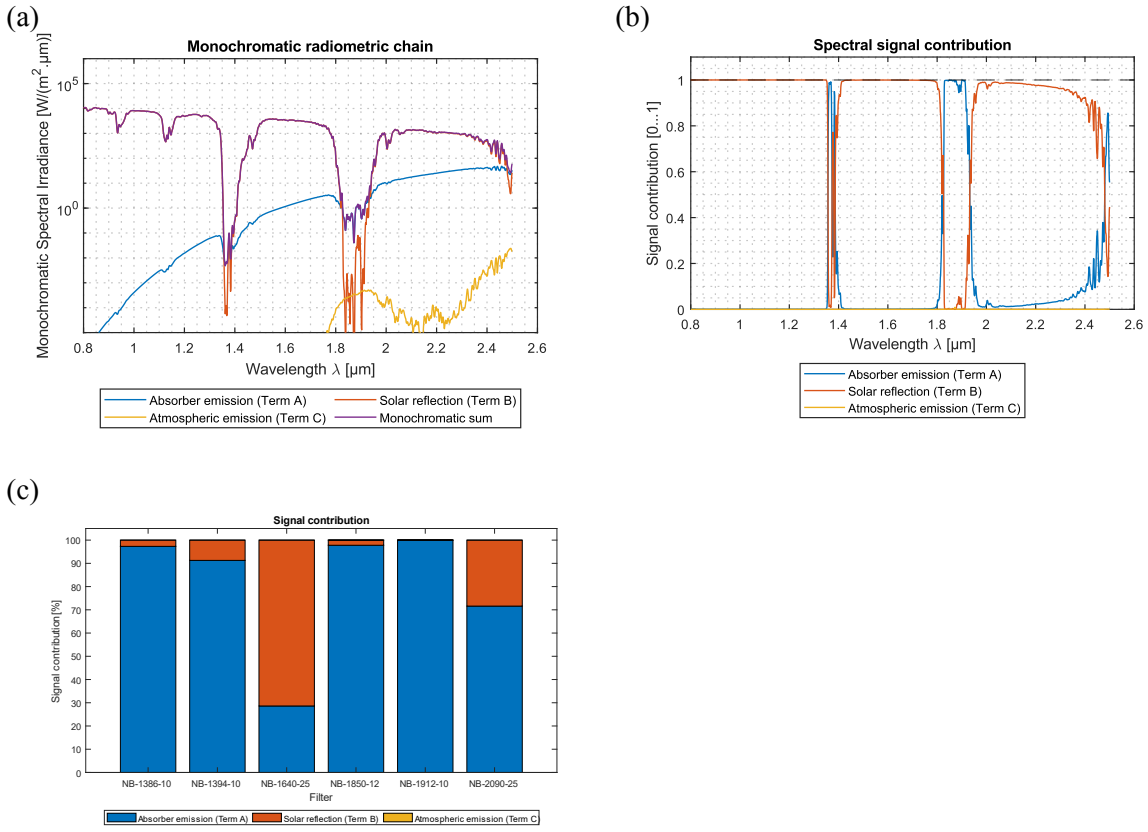

Figure 12: (a): spectral terms absolute contributions, (b): spectral terms relative contributions, (c): integral relative terms contributions; for the following parameters: Coating: Pyromark 2500, $T_{abs} = 600\,°C$, $RH = 30\,\%$, $Cx = 300$, $SZA = 20°$, $L_2 = 500m$, $L_3 = 350\,m$, $P_{atm} = 960\,hPa$, $T_{air} = 30°C$, $H_0 = 500\,m$

Inverse resolution

Average absorber emittance and atmospheric path 3 transmittance will be used in the following. They are computed based on their spectral counterparts (Eq. 17-19):

$$\epsilon = \frac{\int_{\lambda_1}^{\lambda_2} \varepsilon_\lambda(\lambda, T)\, f_{cam}(\lambda)\, M_{\lambda\,\mathrm{BB\,abs}}(\lambda, T)\, d\lambda}{\int_{\lambda_1}^{\lambda_2} f_{cam}(\lambda)\, M_{\lambda\,\mathrm{BB\,abs}}(\lambda, T)\, d\lambda} \quad (18)$$

$$\tau_3 = \frac{\int_{\lambda_1}^{\lambda_2} \tau_{3\,\lambda}(\lambda,T)\, f_{cam}(\lambda)\, M_{\lambda\ \mathrm{BB\ abs}}(\lambda,T)\, d\lambda}{\int_{\lambda_1}^{\lambda_2} f_{cam}(\lambda)\, M_{\lambda\ \mathrm{BB\ abs}}(\lambda,T)\, d\lambda} \quad (19)$$

$$\varepsilon\tau_3 = \frac{\int_{\lambda_1}^{\lambda_2} \varepsilon_\lambda \tau_{3\,\lambda}(\lambda,T)\, f_{cam}(\lambda)\, M_{\lambda\ \mathrm{BB\ abs}}(\lambda,T)\, d\lambda}{\int_{\lambda_1}^{\lambda_2} f_{cam}(\lambda)\, M_{\lambda\ \mathrm{BB\ abs}}(\lambda,T)\, d\lambda} \quad (20)$$

With λ_1 and λ_2 the lower and upper limits defined in Table 1.

Table 1: lower and upper limits of infrared windows

μm	LWIR	SWIR
λ_1	7	0.8
λ_2	14	2.5

Band thermography using LWIR

The LWIR camera uses single wavelength thermography. In single-color or single wavelength thermography, the radiation of the target at one wavelength or band is used to deduce its temperature thanks to Planck's radiation law, provided the surface emittance ϵ_{abs} and the atmospheric transmittance τ_{atm} are known a priori.

The software uses the calibration curve $S_{calib}(T)$ to estimate the signal S_{atm} due to atmospheric radiation from air temperature T_{air} (Figure 13, (22)). This signal is also corrected for absorber emittance ϵ_{abs}, that must be known, and atmospheric transmittance τ_{atm}, that is retrieved in the lookup table. The corrected signal is then projected on the calibration curve to get the absorber temperature T_{abs} (Figure 13, (22)).

$$S_{meas} = \epsilon\tau_3\, \mathrm{S_{calib}}(T_{abs}) + (1-\tau_3)\, \mathrm{S_{calib}}(T_{atm}) \quad (21)$$

$$T_{abs} = S_{calib}^{-1}\left(\frac{S_{meas} - (1-\tau_3)\, \mathrm{S_{calib}}(T_{atm})}{\epsilon\tau_3}\right) \quad (22)$$

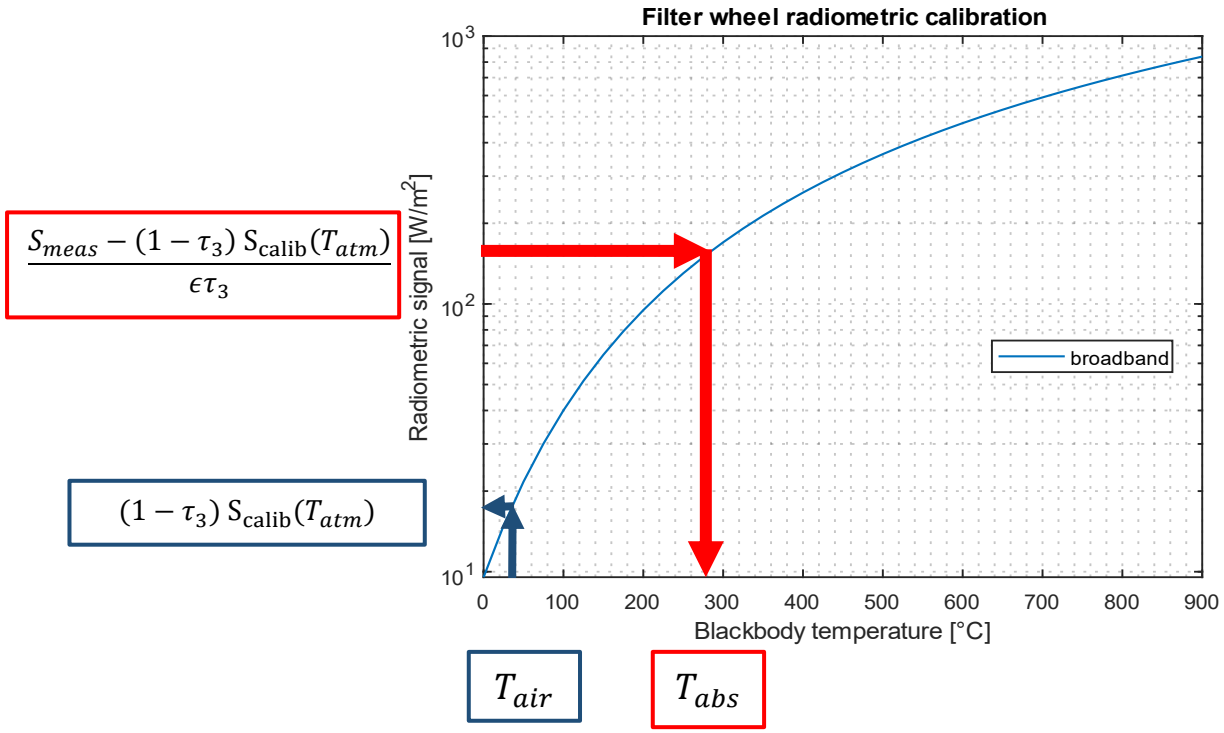

Figure 13: LWIR temperature reading

This method requires knowing the absorber emittance ϵ_{abs} and atmospheric transmittance τ_{atm} beforehand, which may be difficult to achieve, especially in a solar tower configuration. Ratio thermography, or dual wavelength thermography, is a method that aims to overcome this limitation by using two spectral bands instead of one.

Ratio thermography using SWIR

The SWIR camera prototype uses dual wavelength thermography. In dual wavelength thermography, the ratio of radiations at two narrow bands of different wavelengths is used to deduce temperature of the target, without the need to know its emittance. However, emittances need to be equal in both filter bands so that they cancel out in the ratio. The pair of wavelengths must therefore be chosen so that the surface can be considered grey.

Lists of filters and couples used are provided in Table 2 and Table 3.

Table 2: list of SWIR filters

Filter number	Filter name	Water sensitivity
1	NB_1386_10	sensitive
2	NB_1394_10	sensitive
3	NB_1640_25	insensitive
4	NB_1850_12	sensitive
5	NB_1912_10	sensitive
6	NB_2090_25	insensitive
7	broadband	insensitive

Table 3: list of SWIR filter couples

Filter i	Filter j	Water sensitivity
NB_1386_10	NB_1850_12	sensitive
NB_1386_10	NB_1912_10	sensitive
NB_1394_10	NB_1850_12	sensitive
NB_1394_10	NB_1912_10	sensitive
NB_1640_25	NB_2090_25	insensitive

In SWIR, the signal ratio SR is computed and projected on the ratio calibration curve to obtain the absorber temperature (Figure 14):

$$SR = \frac{(S\epsilon\tau_3)_j}{(S\epsilon\tau_3)_i} = \frac{S_j}{S_i}\frac{\epsilon_j}{\epsilon_i}\frac{\tau_{3\,j}}{\tau_{3\,i}} = SR_{meas} NGCF_{abs}\, NGCF_{atm} \quad (23)$$

With:

$$SR_{meas} = \frac{S_j}{S_i} \quad (24)$$

$$NGCF_{abs} = \frac{\epsilon_j}{\epsilon_i} \quad (25)$$

$$NGCF_{atm} = \frac{\tau_{3\,j}}{\tau_{3\,i}} \quad (26)$$

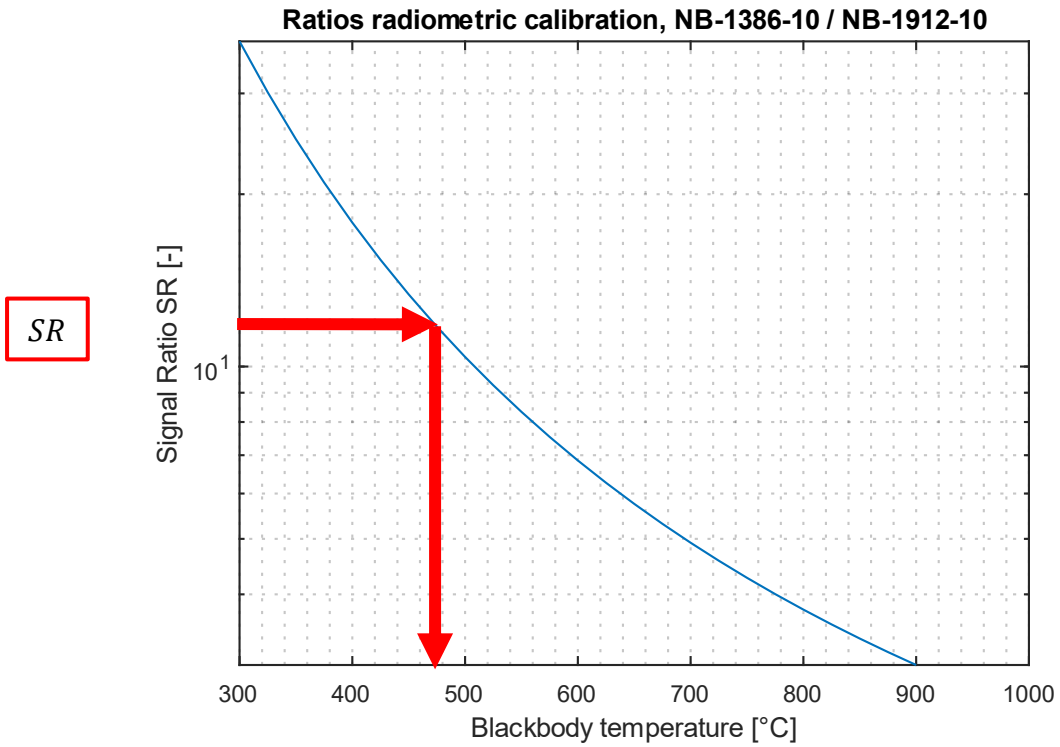

Figure 14: Temperature calculation for dual wavelength thermography

$NGCF_{abs}$ is supposed to be equal to one as the coating of the absorber is deemed to be gray, i.e., to have a constant emittance for all wavelengths. However, $NGCF_{atm}$ is expected to be significantly dependent on atmospheric water vapor, depending on the filter pair selection.

It is then possible to project the estimated temperature on the single wavelength calibration curve of one of the filters to obtain the ideal signal if the absorber were a black body (Figure 15).

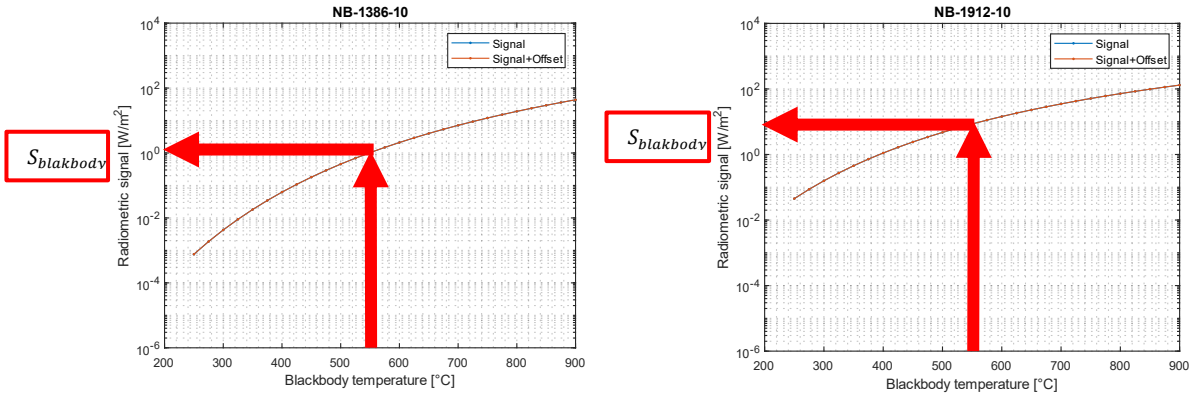

Figure 15: Blackbody signal calculation for: (b) filter NB-1386-10 and (b): filter NB-1912-10

The product of average emittance and atmospheric transmittance for filter i can be computed (Eq.26):

$$(\epsilon\tau_3)_i = \frac{S_i}{S_{BB\,i}} \tag{27}$$

Since average transmittance is already estimated by forward simulation, average emittance can be estimated (Eq. 27):

$$\epsilon_i = \frac{(\epsilon\tau_3)_i}{\tau_{3\,i}} \tag{28}$$

Summary of methodology

The forward problem aims to mimic the actual situation, using provided spectral information. The camera's measured signal is the result of multiplying the total radiometric signal with the total camera spectral response, and then integrating it (radiometric equation). The reference band values for and the reference band emittance-transmittance product $\epsilon\tau_3$ is computed.

The inverse resolution calculates the temperature and emittance. It uses ratio thermography to get the absorber temperature from signal for two filters, corrected by a Non Greybody Compensation Factor (NGCF) computed from MODTRAN simulations.

A theoretical blackbody signal is obtained from the estimated absorber temperature thanks to the filter calibration curve. The emittance is then computed using the reference band emittance-transmittance product $\epsilon\tau_3$ from the forward problem and the theoretical blackbody signal.

The methodology is summarized in a flowchart Figure 16.

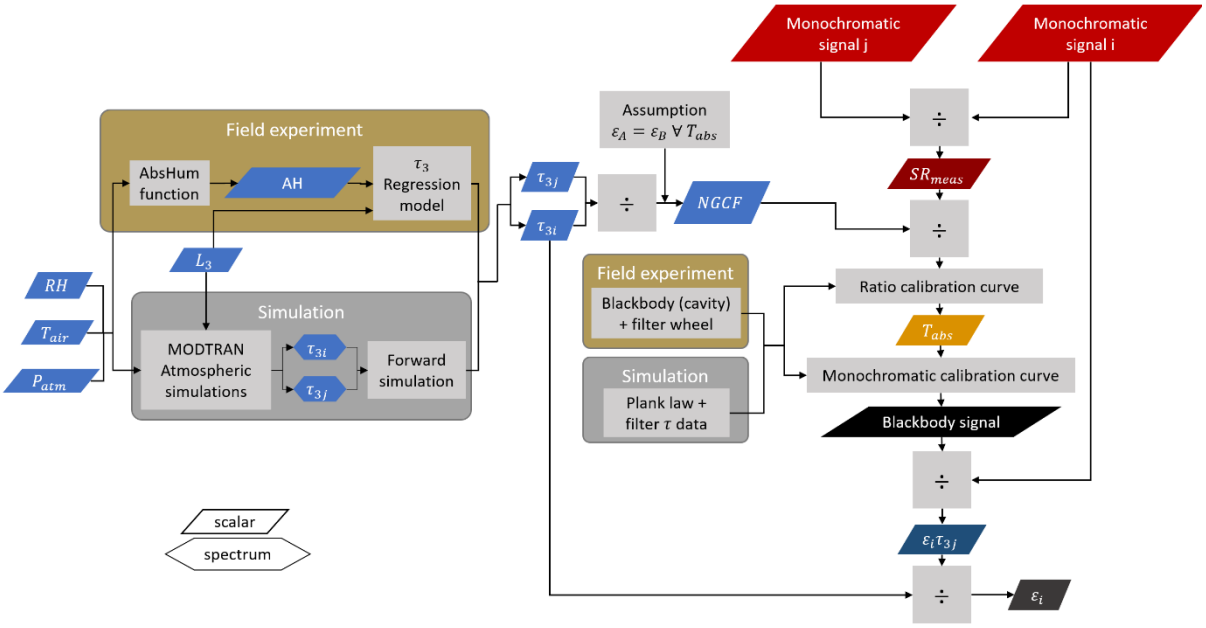

Figure 16: flowchart of SWIR temperature and emittance calculations

Results and Discussion

This chapter presents and analyses the results from the DOE simulations to analyze the influence of atmospheric water vapor absorption on the precision and accuracy of infrared temperature measurements (SWIR, LWIR) in the context of the solar tower of Cerro Dominador, Chile. Other relevant parameters related to the power plant are also examined, to identify other criteria that are necessary for accurate measurements.

Analysis of LWIR configuration

Atmospheric transmittance

Knowledge of atmospheric transmittance on path 3 is key to reduce measurement error as it affects the amount of radiation that reaches the camera.
Figure 17 illustrates how the atmospheric transmittance of path 3, varies with the absolute humidity and the length of path 3. The graph shows that the atmospheric transmittance of path 3 decreases as both the absolute humidity and the length of path 3 increase. This means that more radiation is lost due to atmospheric effects when the air is more humid, and the path is longer. The lower the path 3 transmittance is, the lower the amount of radiation emitted by the absorber reaches the camera. This means that the atmospheric emission and scattering term takes importance as τ_3 decreases.

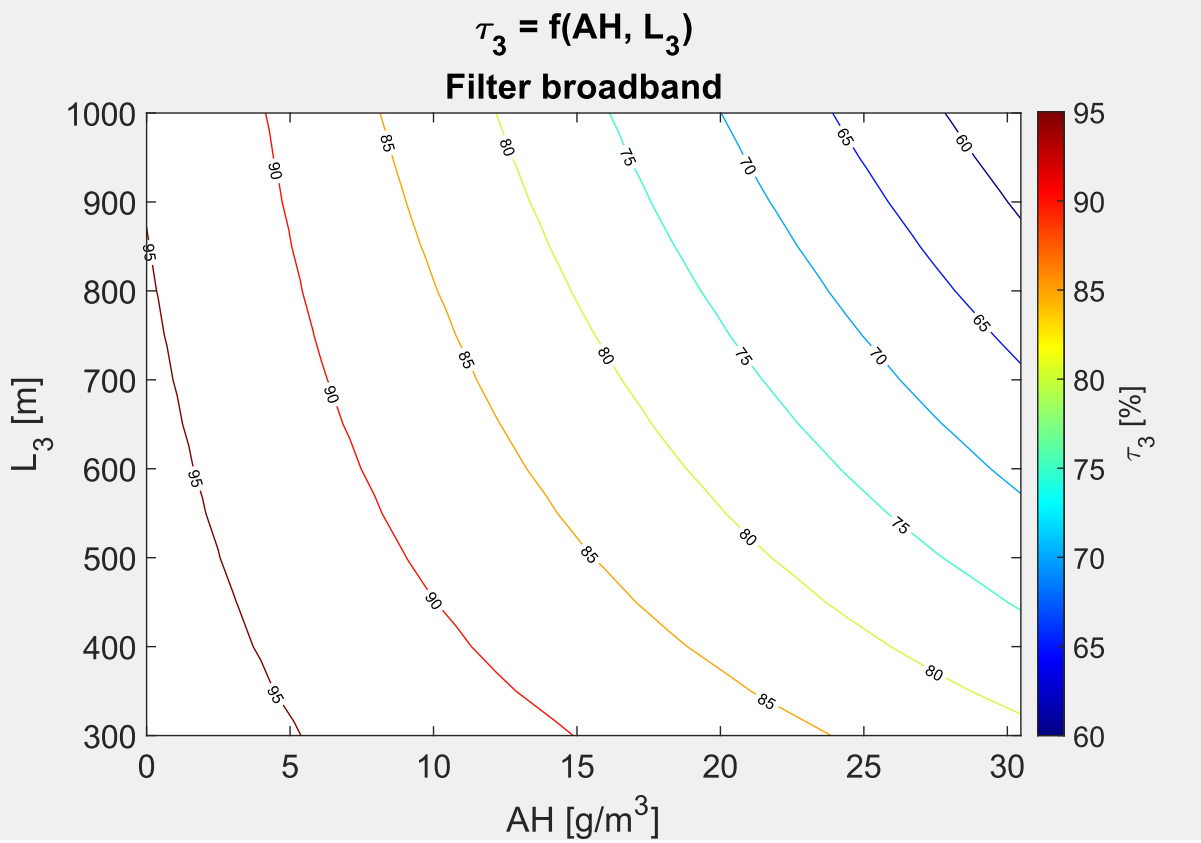

Figure 17: influence of absolute humidity and length of path 3 on atmospheric transmittance of path 3; for $T_{air} = 30\ °C$

Relative error and solar blindness

Solar blindness helps reduce solar perturbation that reflects on the absorber.
Figure 18 shows a positive correlation between absolute humidity and optical atmospheric depth, meaning that higher humidity leads to more attenuation of solar radiation. There is also a negative correlation between solar zenith angle and optical atmospheric depth, meaning that lower angles (when the sun is higher in the sky) lead to less attenuation of solar radiation.

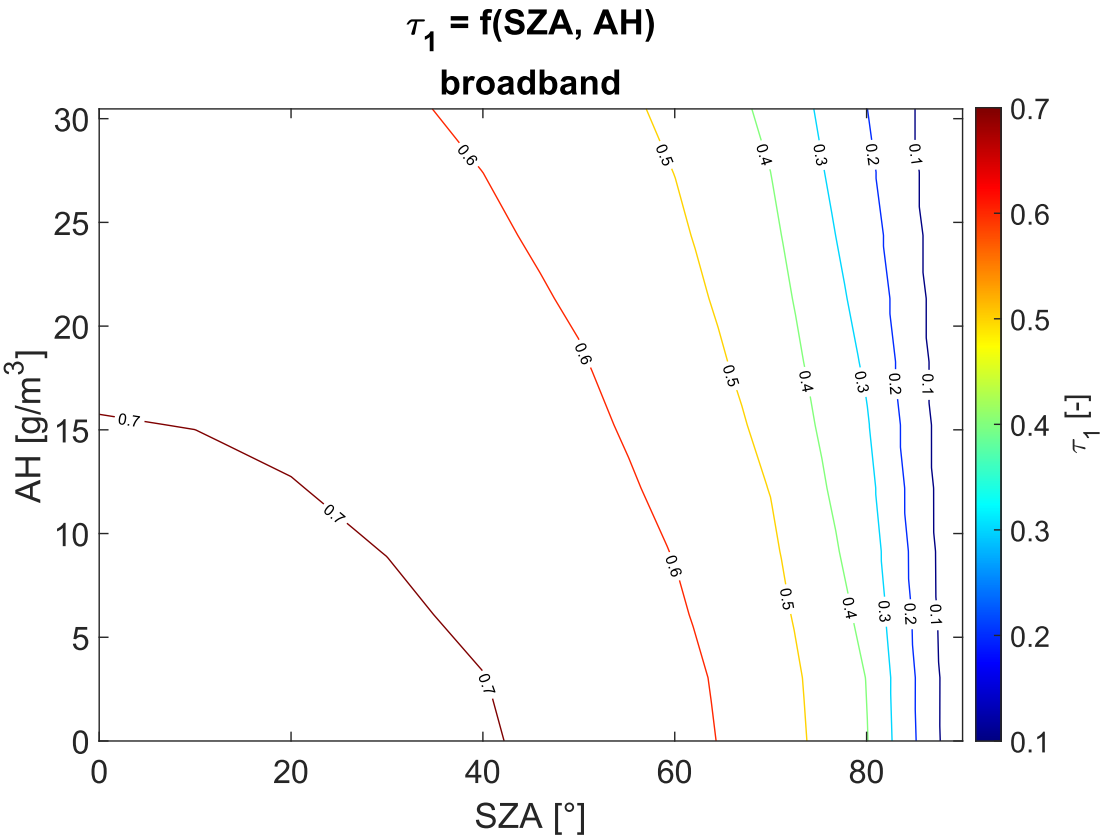

Figure 18: influence of absolute humidity and solar zenith angle on atmospheric transmittance for LWIR system; for $T_{air} = 30\ °C$

Solar blindness is deemed satisfied when the amount of solar radiation reaching the camera is negligeable compared to the radiation emitted by the absorber. However, it is difficult to determine a fixed threshold for acceptable values of solar radiation because the problem does not only depend on path 1 transmittance. Solar blindness is therefore considered equivalent with relative error, which is the final and main result. Sources of errors in the relative temperature error are the uncertainty of true atmospheric composition, as it is estimated with models from ground sensors, and solar perturbation. Since simulations do not consider atmospheric uncertainty, solar blindness is equivalent to relative temperature error.

Figure 19 shows acceptable relative errors for all values of absolute humidity, absorber temperature and concentration factor. This is consistent with the low solar irradiance in the LWIR spectrum, minimizing solar perturbation on the measurement.

However, relative error increases with concentration factor and decreases with absorber temperature and absolute humidity. Solar perturbation remains present in minor quantity.

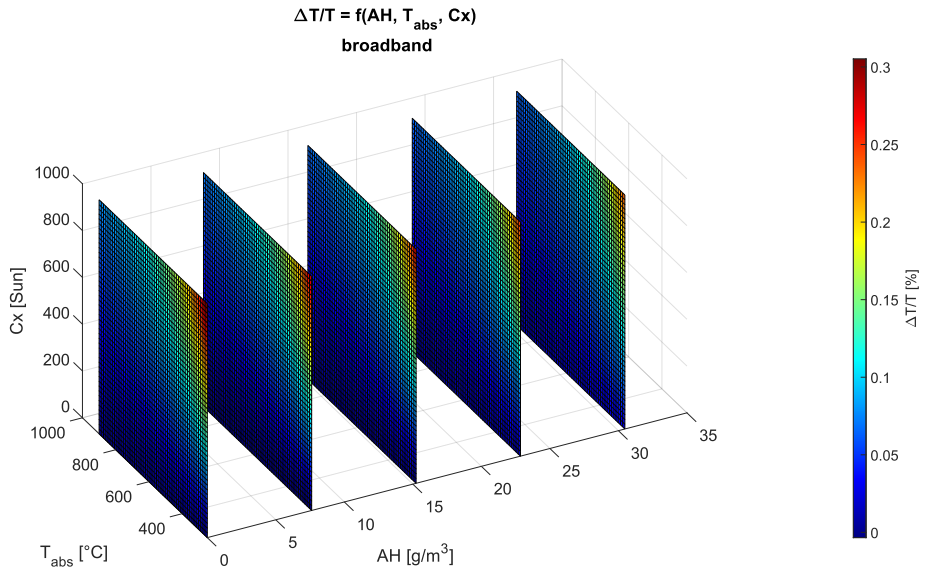

Figure 19: influence of absolute humidity, absorber temperature and concentration factor on relative temperature error; for Coating: Pyromark 2500, $T_{air} = 30\ °C$ and $L_3 = 350\ m$

This section has presented the results of the simulation of the LWIR system for different atmospheric and operational conditions. The relative temperature error is acceptable for all values of absolute humidity, absorber temperature and concentration factor. This indicates that the LWIR system is not significantly affected by solar perturbation.
This suggests that the LWIR system is a viable option for measuring the absorber temperature in CSP plants, as it can achieve accurate results under various atmospheric and operational conditions.

Analysis of SWIR configurations

Correction function for laboratory calibrations

More importantly than for LWIR, knowledge of atmospheric transmittance on path 3 is key to reduce SWIR measurement error as it affects greatly the amount of radiation that reaches the camera.

Figure 20 and Figure 21 show that path 3 transmittance decreases with absolute humidity for most filters. These filters are called water-sensitive filters (NB-1386-10, NB-1394-10, NB-1850-12 and NB-1912-10, see Table 2). The atmospheric transmittances for the two other filters are not affected by absolute humidity AH. This is consistent with Figure 4, where the atmosphere shows absorption bands at wavelengths corresponding to water-sensitive filters. A numeric correlation is given in Appendix A.

Transmittances for the two filters of a couple often are not identical. This discrepancy will affect ratio thermography as described in (23). Therefore, the NGCF is needed to compensate for this difference in τ_3.

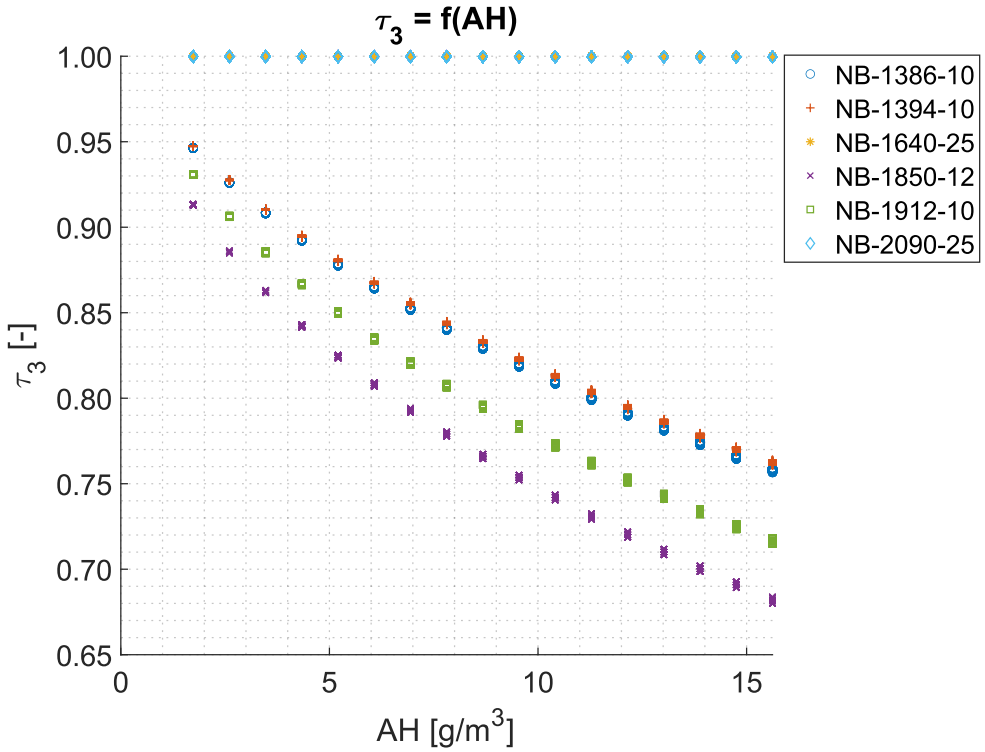

Figure 20: influence of absolute humidity on air transmittance for each filter, **laboratory** (range: 7 meters); for the following parameters: $T_{air} = 20\ °C$, $L_3 = 7\ m$, $Cx = 0$, $P_{atm} = 960\ hPa$

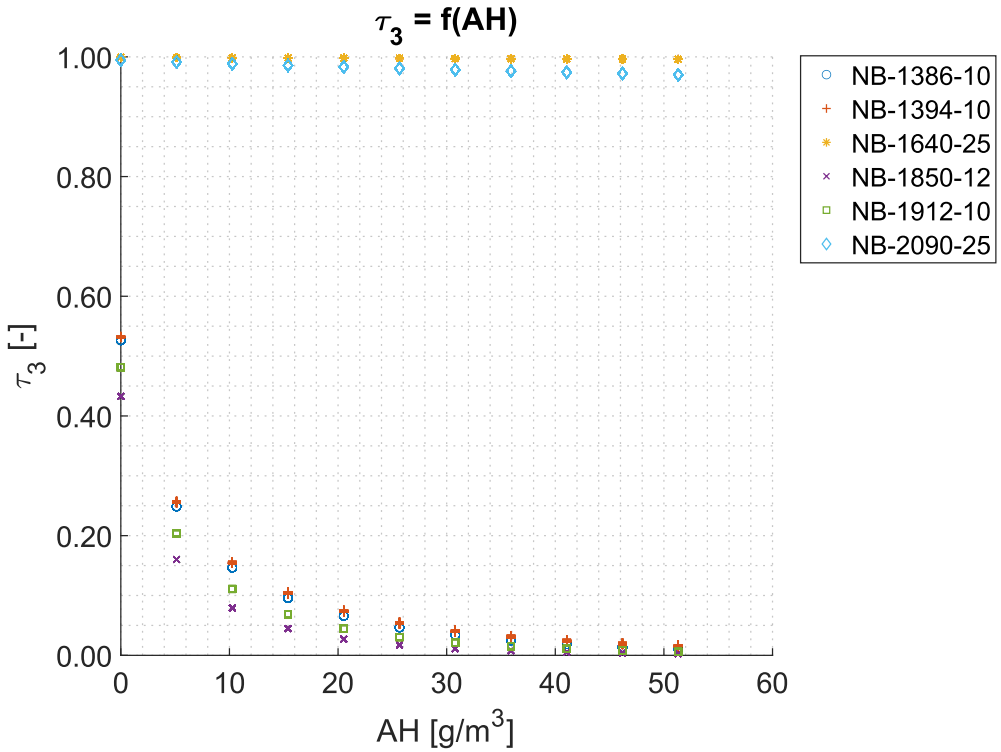

Figure 21: influence of absolute humidity on air transmittance for each filter, **tower** (range: 350 meters); for the following parameters: $T_{air} = 40\ °C$, $L_3 = 350\ m$, $Cx = 0$, $P_{atm} = 850\ hPa$

Criteria for solar blindness on the field

Optical depth, a logarithmic form of path 1 transmittance, indicates the attenuation of solar perturbation by atmosphere on path 1. Figure 22 shows that, for the couple of filters NB-1386-10 and NB-1912-10, atmospheric transmittance on path 1 is low, and decreases with absolute humidity and solar zenith angle (increases as the sun rises in the sky). This is explained by a longer path through atmosphere as this path leaves the normal to the atmosphere.

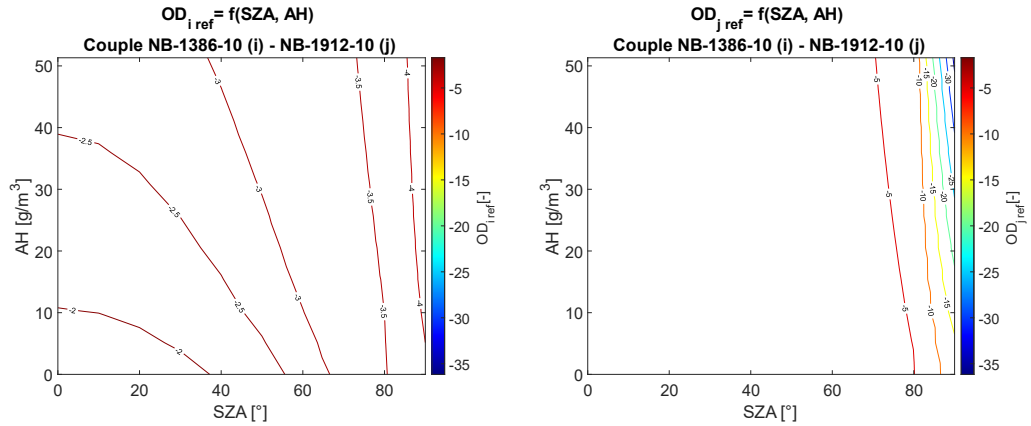

Figure 22: influence of absolute humidity and solar zenith angle on optical depth for a couple of water-sensitive filters

Figure 23 shows that, for the water-insensitive couple of filters NB-1640-25 and NB-2090-25, atmospheric transmittance on path 1 is high, also decreasing with absolute humidity and solar zenith angle. This makes this couple suitable only for off-sun measurements, as solar perturbation is otherwise too high.

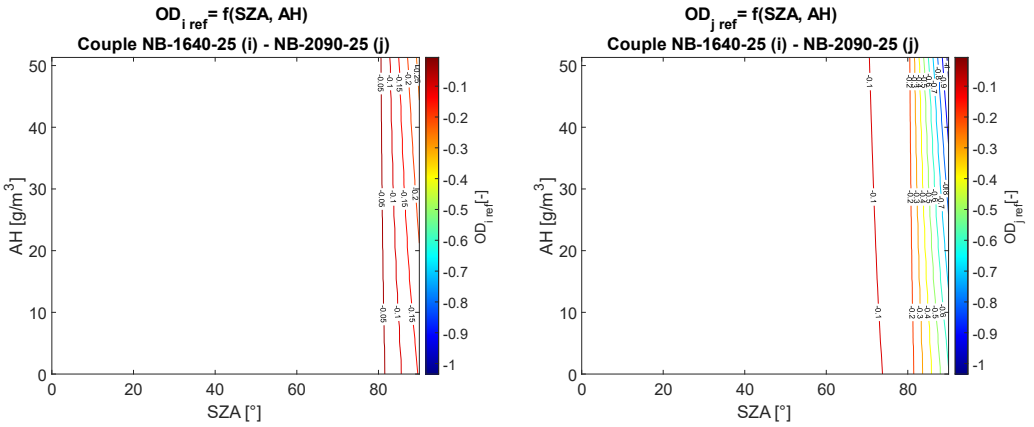

Figure 23: influence of absolute humidity and solar zenith angle on optical depth for a couple of water-insensitive filters

Relative error

Relative error is the measure that will determine if, in a set of conditions, the accuracy of the measurement is satisfactory. A general view of the influence of each variable on relative error is presented on Figure 33 in Appendix B.

Figure 24 shows that the accuracy of the measurement greatly depends on the absorber temperature. At the specified parameters, measurements below 400 °C are impractical. At low absolute humidities, this threshold lowers as the sun goes down. However, the higher the absolute humidity, the less solar zenith angle impacts accuracy, and the higher absorber temperature is needed.

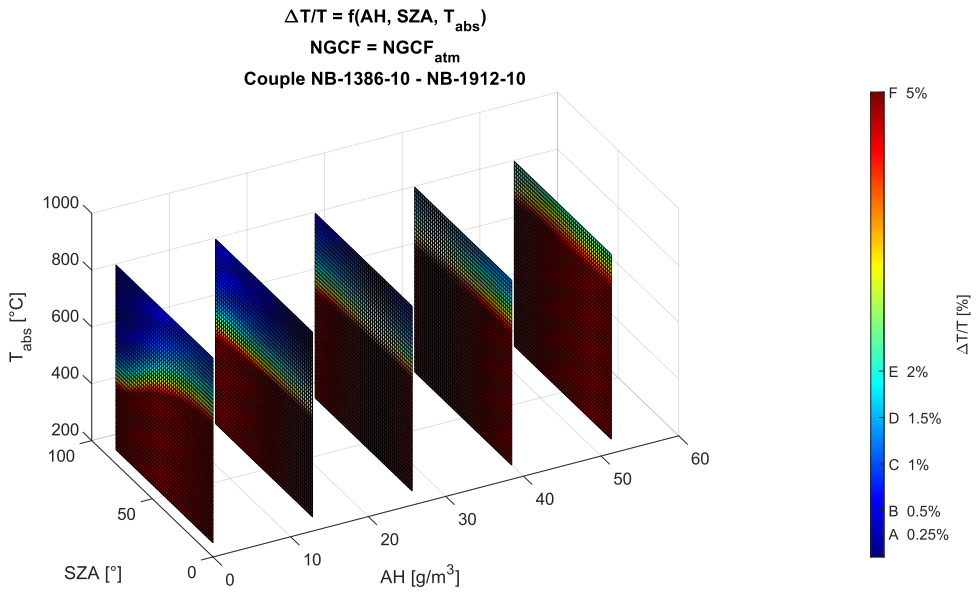

Figure 24: influence of absolute humidity, solar zenith angle and absorber temperature on relative temperature error for a water-sensitive couple of filters; for the following parameters: $T_{air} = 40\ °C$, $Cx = 1000$, $L_3 = 350\ m$

Figure 25 shows accuracy of temperature measurement for dusk conditions. The reason dusk conditions were chosen is that for a couple of water-insensitive filters, solar radiation would not be filtered by the atmospheric water vapor, because these filters let through radiation at wavelengths atmosphere is transparent.

As expected for water-insensitive filters, temperature accuracy does not depend on absolute humidity. It does depend on absorber temperature. However, the accuracy is still very good. Accuracies at dusk are shown in Figure 36 on Appendix C.

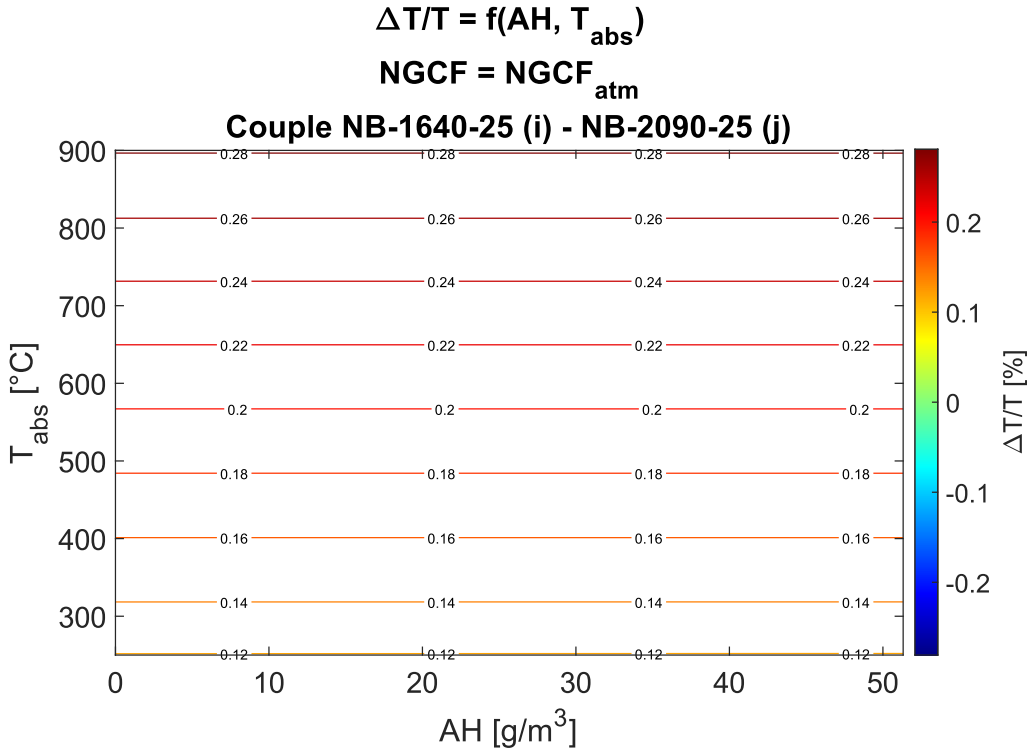

Figure 25: relative temperature error for a couple of water-insensitive filters; for the following parameters: $T_{air} = 40\ °C$, $Cx = 0$, $L_3 = 350\ m$, $SZA = 90\ °$

Non-gray compensation factor on the field

Atmospheric conditions are not well known but derived from measurements on the ground. To minimize uncertainty on temperature readings, influence of atmospheric transmittance must be minimized, thus NGCF must be maximized. Indeed, the more NGCF is close to one, the less atmospheric transmittance affects simulations.

Furthermore, NGCF varies with absorber temperature due to Wien's displacement law, as depicted on Figure 27 and Figure 28, and causing Figure 26 to have several values of NGCF for the same filter and the same absolute humidity. Indeed, the influence of absorber temperature on τ_3 caused by Wien's displacement law also occurs on $NGCF_{atm}$ as shown in (26).

The water-sensitive couple with the highest $NGCF_{atm}$ is the couple NB-1386-10 – NB-1912-10. This couple also happens to be the least sensitive to absorber temperature. Correcting atmospheric discrepancies in the field will be easier as NGCF only depends on absolute humidity.

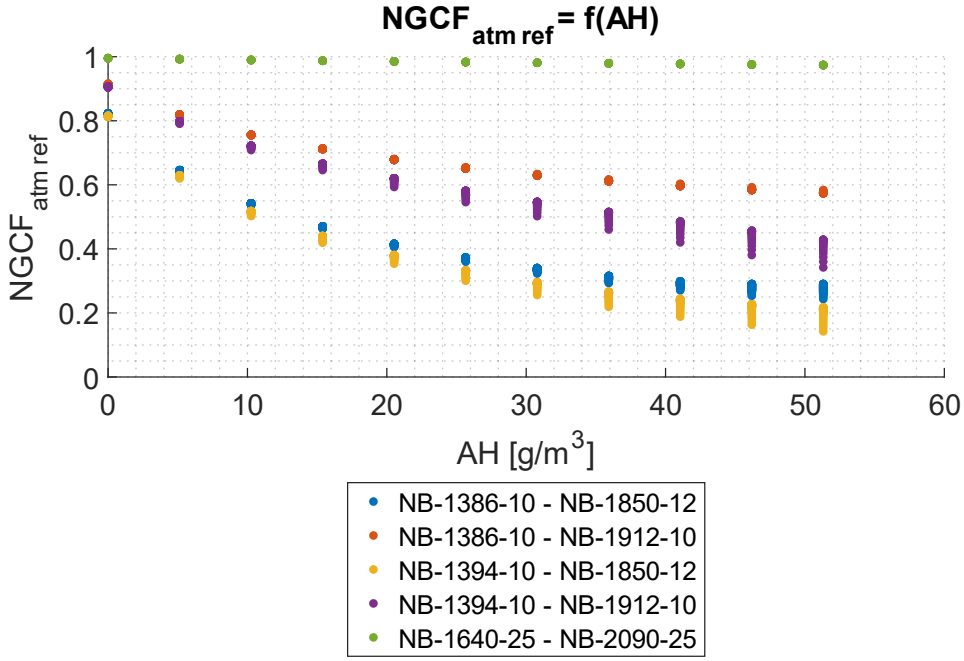

Figure 26: influence of absolute humidity on atmospheric NGCF; for the following parameters: $L_3 = 350\ m$, $\Delta T/T \leq 2\%$, $T_{air} = 40\ °C$, $SZA = 0\ °$

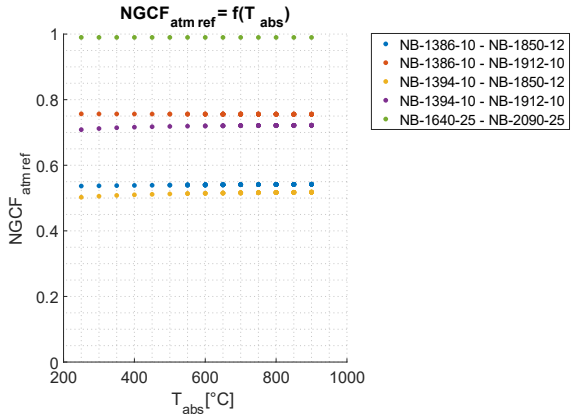

Figure 27: influence of absorber temperature on $NGCF_{atm}$; for the following parameters: $L_3 = 350\,m$, $\Delta T/T \leq 2\%$, $T_{air} = 40\,°C$, $SZA = 0\,°$, $AH = 10\,g/m^3$

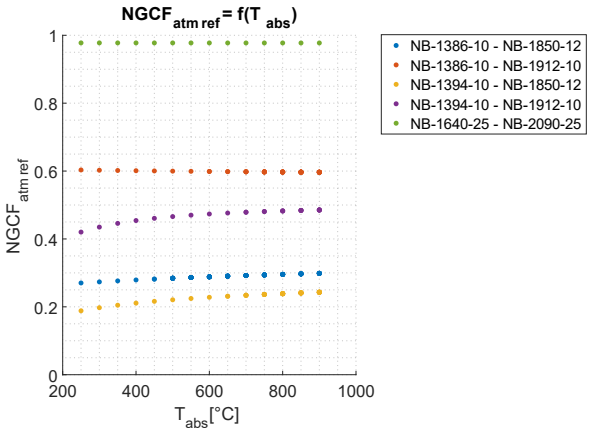

Figure 28: influence of absorber temperature on $NGCF_{atm}$; for the following parameters: $L_3 = 350\,m$, $\Delta T/T \leq 2\%$, $T_{air} = 40\,°C$, $SZA = 0\,°$, $AH = 41\,g/m^3$

Emittance vs. Temperature error correlation

A correlation between temperature relative error and emittance absolute error is useful to easily determine emittance error with only one input that is relative temperature error. It can be established by displaying all simulations results on a scatter plot. Several lines, corresponding to several values of absorber temperature emerge from Figure 29.

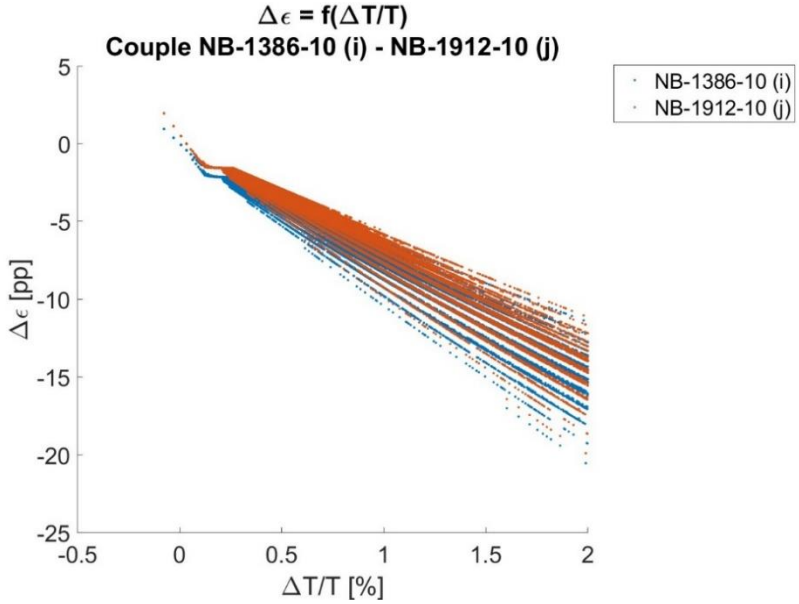

Figure 29: correlation between relative temperature error and emittance error for a water-sensitive couple of filters; for $L_3 = 350\ m$

For a water-sensitive couple of filters and an absorber temperature of 600 °C, a percent of relative error on absorber temperature induces an absolute emittance error of 8 percentage points (Figure 30).

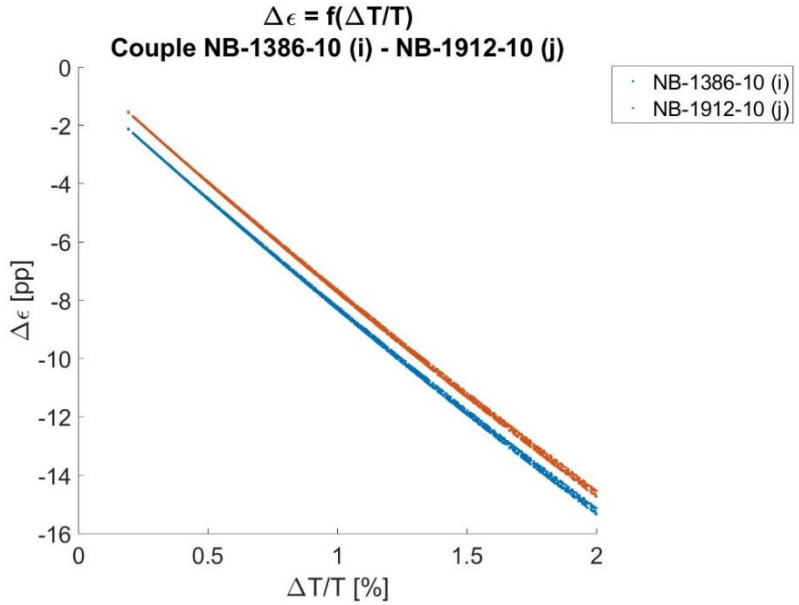

Figure 30: correlation between relative temperature error and emittance error for a water-sensitive couple of filters; for $L_3 = 350\ m$ and $T_{abs} = 600\ °C$

For a water-sensitive couple of filters and an absorber temperature of 400 °C, a percent of relative error on absorber temperature induces an absolute emittance error of 10 percentage points (Figure 31).

As relative temperature error decreases as absorber temperature increases, making difficult low temperature measurements, emittance absolute error follows the same trend: it increases as absorber temperature decreases.

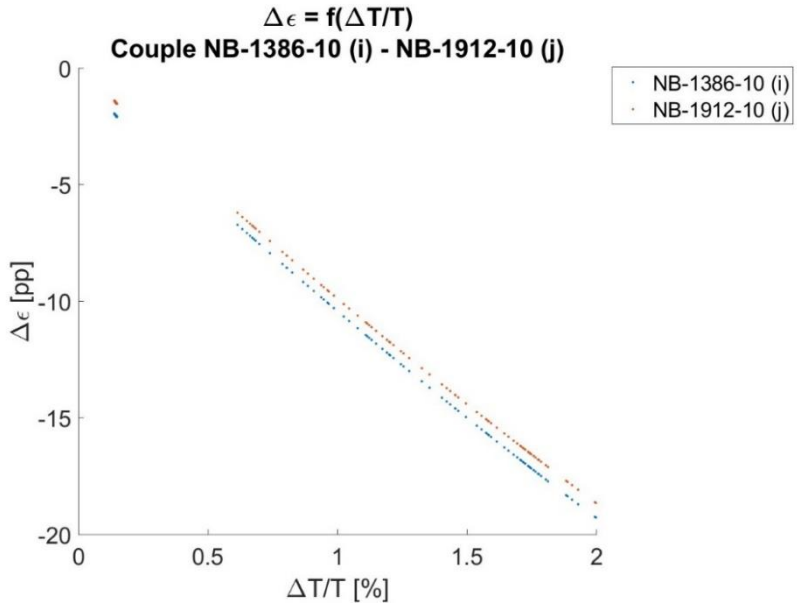

Figure 31: correlation between relative temperature error and emittance error for a water-sensitive couple of filters, for $L_3 = 350\ m$ and $T_{abs} = 400\ °C$

Figure 32 shows that, for the water-insensitive couple of filters, absolute emittance error is lower than for a water-sensitive couple: within 2 percentage points. It slightly increases with relative temperature error.

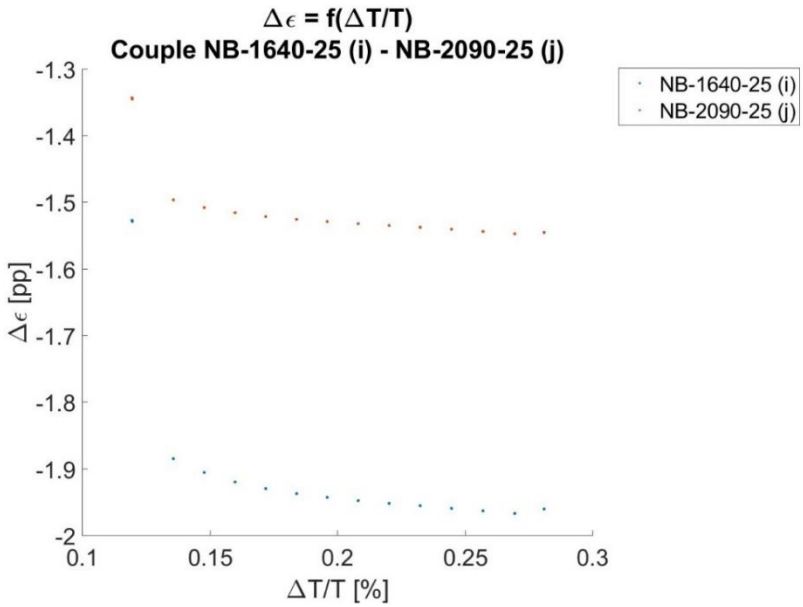

Figure 32: correlation between relative temperature error and emittance error for a water-insensitive couple of filters; for $L_3 = 350\ m$

The water-insensitive couple of filters shows good accuracies on both temperature measurements and emittance measurements, but requires to be operated at dusk, i.e., without direct solar irradiance. When operating at dusk, it is nonetheless the best suited, as it does not depend on uncertainties on atmospheric transmittance due to the estimation, from measurements on the ground, of air temperature and humidity along the path of the radiation.

The selected water-sensitive couple of filters can obtain measurements with good accuracies on absorber temperature for a constrained set of parameters. The most important parameter is absolute humidity, with an ideal value around $10\ g/m^3$.

However, the correlation between all the parameters and the relative temperature error cannot be accurately described in a simple way. The great influence of relative temperature error on emittance error restricts even more the set of parameters, thus the occasions to measure with accuracy on the field.

It is yet possible to build a tool that interpolates simulation results to obtain the relative temperature error. This tool is used to estimate real world relative error with weather and solar data and indicates that, for conditions encountered at the tower of Cerro Dominador, Chile, water-sensitive filters do not provide sufficient accuracies in the day. Measurements at dusk are therefore necessary, which makes the water-insensitive couple superior as it depends less than water-sensitive ones on atmospheric transmittance, thus decreasing its sensibility to atmospheric uncertainties.

Conclusion

The main objective of this work was to determine the effect of atmospheric water vapor absorption on the precision and accuracy of infrared temperature measurements in the context of industrial solar towers. To achieve this goal, a software tool was developed and improved for the compensation of atmospheric effects on infrared measurements. The tool used dual wavelength thermography and non-graybody compensation factor as corrections of theoretical measurements. The tool also incorporated a simulation code that used the atmospheric simulation software MODTRAN to model the air transmittance under different conditions. The tool was used to visualize and analyze the influence of various factors, such as altitude, atmospheric pressure, air temperature, relative humidity, ray path length, and atmospheric perturbation, on the air transmittance and the temperature reading errors. The tool was also applied to a real tower scenario at the Cerro Dominador solar furnace in Chile, where historic weather data was used to determine the best time to conduct experiments. Models were built to estimate atmospheric transmittances and temperature relative errors without relying on new simulations.

The thesis has investigated the performance of two different SWIR systems and one LWIR system for measuring the absorber temperature in CSP plants. The simulation results have shown that the LWIR system is robust to solar perturbation and can achieve accurate temperature measurements for various atmospheric and operational conditions. The SWIR systems, on the other hand, are more sensitive to water vapor and solar irradiance, and require specific conditions to obtain reliable results. The water-insensitive SWIR system is preferable to the water-sensitive one, as it does not depend on the estimation of atmospheric transmittance and can operate at dusk without direct solar irradiance. The water-sensitive SWIR system can only provide satisfactory measurements for a limited range of parameters, which can be determined by using an interpolation tool based on the simulation data. Therefore, the thesis concludes that the LWIR and water-insensitive SWIR system are the most suitable options for measuring the absorber temperature in CSP plants, the latter being cheapest but not suitable for real time operation. The water-sensitive SWIR system is not viable unless the atmospheric and operational conditions are favorable.

The thesis has also identified some limitations and possible future improvements for the temperature measurement systems. One of them is to consider the effect of aerosols on atmospheric transmittance, as they can scatter and absorb the radiation and alter the measurements, at least in the SWIR range. Another one is to use more accurate models of the atmospheric parameters' profiles along the altitude, such as temperature, pressure, and humidity, to determine the transmittance with better precision. A third one is to study the influence of the uncertainties of atmospheric parameters on NGCF and on the relative temperature error, and to propose methods to reduce or compensate for these uncertainties. These future improvements could enhance the performance and reliability of the temperature measurement systems and provide more accurate data for CSP plants.

References

[1] https://www.irena.org/Energy-Transition/Technology/Solar-energy.

[2] https://cdn.website-editor.net/s/6dda707ea3f04fbf9ec53cc8b4bb79ad/files/uploaded/EN%2520211116_DCSP_Kurzstudie_online_EN.pdf?Expires=1693325650&Signature=bRb4fJ-zCFxWloDSOGYBasW0~mzwePwi~BmVShNHxXVa31nHg9do3Eu-AR7zNq-fQwaq12A5oxrqBvZN0MenVIvbF-M2zgz~3BLWo.

[3] https://www.solarpaces.org/how-csp-works/.

[4] https://www.infratec.eu/thermography/industrial-automation/solar-power-tower-check-sptc/.

[5] Hernandez, D., et al. "Analysis and experimental results of solar-blind temperature measurements in solar furnaces." J. Sol. Energy Eng. 126.1 (2004): 645-653. https://doi.org/10.1115/1.1636191.

[6] Johnson, Harold L., and W. W. Morgan. "Fundamental stellar photometry for standards of spectral type on the revised system of the Yerkes spectral atlas." The Astrophysical Journal 117 (1953): 313. https://ui.adsabs.harvard.edu/link_gateway/1953ApJ...117...

[7] Caron, Simon, et al. "Forty shades of black: A benchmark of high temperature sprayable black coatings applied on Haynes 230." AIP Conference Proceedings. Vol. 2303. No. 1. AIP Publishing, 2020. https://doi.org/10.1063/5.0028773.

[8] Hijazi, A., et al. "A calibrated dual-wavelength infrared thermometry approach with non-graybody compensation for machining temperature measurements." Measurement Science and Technology 22.2 (2011): 025106. http://dx.doi.org/10.1088/0957-0233/22/2/025106.

[9] Eitan, A., et al. "Accurate flux calculations using thermographic IR cameras in concentrated solar power fields." Quantitative InfraRed Thermography (QIRT) International Conference Proceedings, Bordeaux. 2014. http://dx.doi.org/10.21611/qirt.2014.220.

[10] Savino, L., et al. "Free emissivity temperature investigations by dual color applied physics methodology in the mid-and long-infrared ranges." International Journal of Thermal Sciences 117 (2017): 328-341. https://doi.org/10.1016/j.ijthermalsci.2017.03.02.

[11] Araújo, A. "Multi-spectral pyrometry—a review." Measurement Science and Technology 28.8 (2017): 082002. https://doi.org/10.1088/1361-6501/aa7b4b.

[12] Pfänder, Markus, Eckhard Lüpfert, and Peter Heller. "Pyrometric temperature measurements on solar thermal high temperature receivers." (2006): 285-292. https://doi.org/10.1115/1.2210499.

[13] https://en.wikipedia.org/wiki/Planck_relation.

[14] Vollmer, M. (2021). Infrared thermal imaging. In Computer Vision: A Reference Guide (pp. 666-670). Cham: Springer International Publishing. https://doi.org/10.1007/978-3-030-63416-2_844.

[15] https://en.wikipedia.org/wiki/Planck's_law.

[16] https://en.wikipedia.org/wiki/Wien%27s_displacement_law.

[17] https://en.wikipedia.org/wiki/Sakuma%E2%80%93Hattori_equation.

[18] https://en.wikipedia.org/wiki/Kirchhoff%27s_law_of_thermal_radiation.

[19] https://en.wikipedia.org/wiki/Solar_irradiance.

[20] http://modtran.spectral.com/modtran_faq.

[21] Maione, B. D., Baldridge, C., & Kudenov, M. W. (2019). Microbolometer with a multi-aperture polymer thin-film array for neural-network-basedtarget identification. Applied Optics, 58(27), 7285-7297. https://doi.org/10.1364/AO.58.007285.

Appendix A

For the filter couple NB_1386_10 - NB_1912_10 and $L_3 = 7\ m$, the regression gives, with $r^2 = 0.996$:

$$\tau_3 = 1 - 2.12\ L_3\ AH + 2488\ L_3^2 + 2.52 \cdot 10^{-5}\ AH^2 + 62.19\ L^2\ AH + 0.018\ L\ AH^2 - 1.2818 \cdot 10^5\ L^3 \quad (29)$$

Appendix B

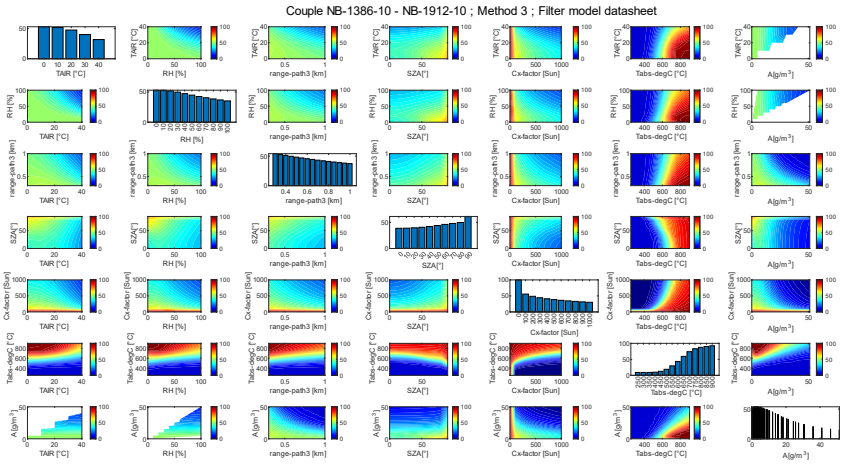

Figure 33: matrix plot of proportion [%] of simulations with relative temperature error below 2 % for a couple of water-sensitive filters

Appendix C

Weather report

Figure 34 shows the best times in the year to operate the water-sensitive couple of filters NB-1386-10 - NB-1912-10. Despite short term perturbations, the best period of the year seems to lay between May and July. This corresponds to the winter season in Chile.

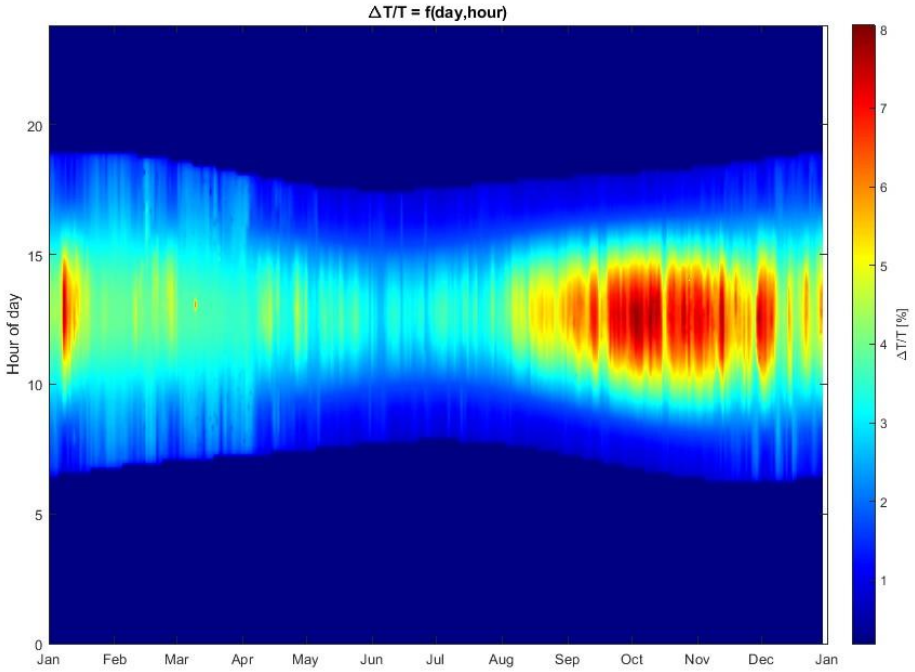

Figure 34: relative temperature error as function of time of year for a water-sensitive couple of filters (NB-1386-10 and NB-1912-10), Cerro Dominador, Chile

However, Figure 35 shows more precisely that the 2% error threshold is always exceeded during most of the day. It is necessary to study measurement accuracy at dusk.

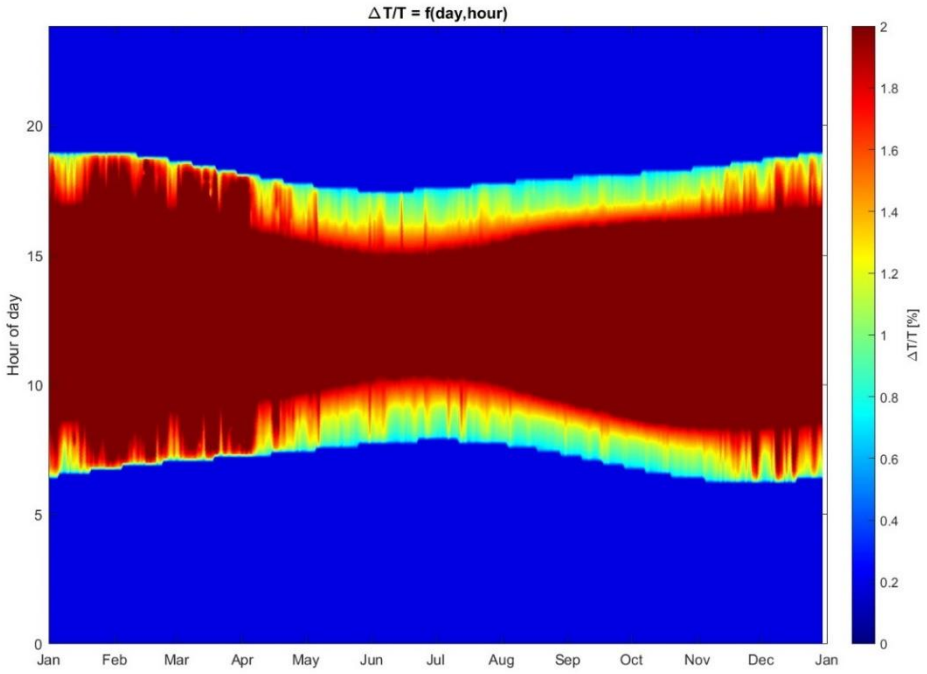

Figure 35: relative temperature error as function of time of year for a water-sensitive couple of filters (NB-1386-10 and NB-1912-10), Cerro Dominador, Chile

Figure 36 shows the relative error at dusk for each couple of filters, considering the weather data. While the water-insensitive couple of filters has the greatest relative error, it is still the best to use at dusk because it minimizes the uncertainties due air humidity while maintaining a good accuracy.

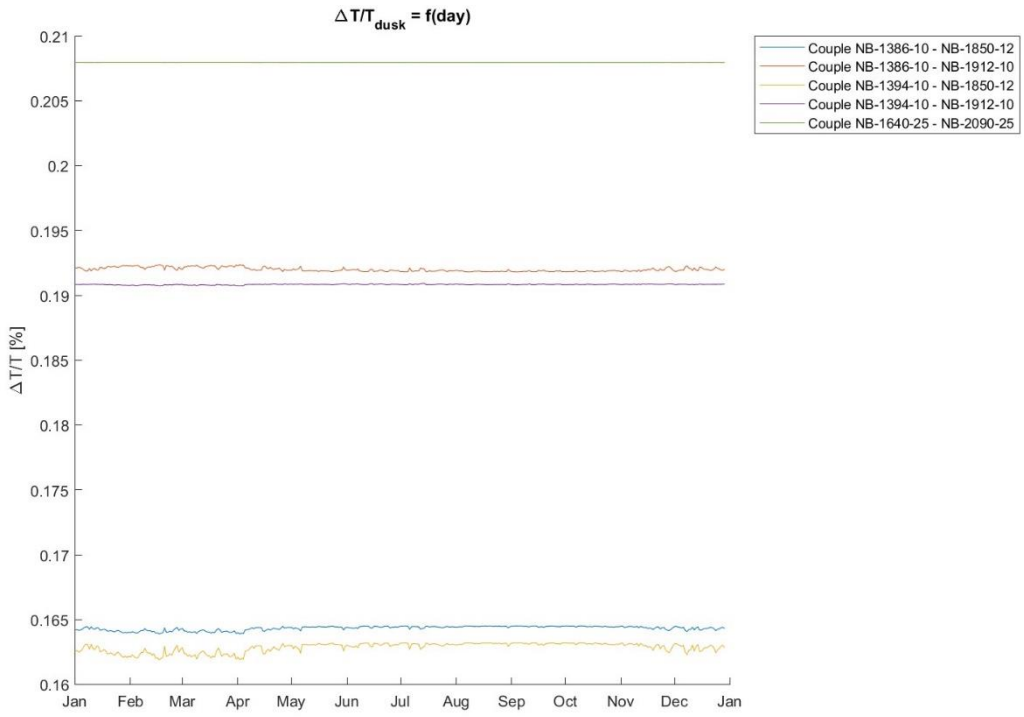

Figure 36: relative temperature error at dusk at Cerro Dominador, Chile